Science and Technology Indonesia
e-ISSN:2580-4391 *p*-ISSN:2580-4405
Vol. 11, No. 3, July 2026

Research Paper

Polysaccharide-Stabilized Butterfly Pea Flower (*Clitoria ternatea*) Anthocyanin as Natural Photosensitizer against MRSA: In Silico and In Vitro Evaluation

Siti Humairoh[1], M. Akram[1], Rumiyati Dwi Nindi Marrisca[1], Aisyah Pratiwi[1], Ade Fadilah[1], Mardiyanto[1,2], Miksusanti[1], Najma Annuria Fithri[1,2*]

[1]*Department of Pharmacy, Faculty of Mathematics and Natural Sciences, Universitas Sriwijaya, Indralaya, South Sumatra, 30682, Indonesia*
[2]*Research Group of Drug Delivery and Nanomaterial Fabrication, Department of Pharmacy, Faculty of Mathematics and Natural Sciences, Universitas Sriwijaya, Indralaya, South Sumatra, 30682, Indonesia*
*__Corresponding author__: najma.fithri@mipa.unsri.ac.id

Abstract
Butterfly pea flower (*Clitoria ternatea*) anthocyanins have potential as natural photosensitizers for photothermal–photodynamic therapy (PTT/PDT) against Methicillin-resistant *Staphylococcus aureus* (MRSA), but their inherent instability under pH and thermal stress limits therapeutic utility. This study evaluated polysaccharide-based stabilization systems for butterfly pea anthocyanin extract (BPFE) and assessed their photosensitizer performance through *in silico* and *in vitro* approaches. Dried flower extraction using 60% ethanol with 30-minute maceration and 45-minute ultrasonic-assisted extraction yielded a total anthocyanin content of 5.037 ± 0.395 mg CGE/L with a photothermal efficiency of 52.34 ± 7.93% at 450 nm and 22.21 ± 2.35% at 550 nm. Molecular docking against penicillin-binding protein 2a or PBP2a (PDB: 1MWU) showed that all 18 screened compounds demonstrated binding affinities of -7.4 to -11.1 kcal/mol. The extract at 8% produced an inhibition zone of 10.67 ± 0.94 mm against *S. aureus* ($p < 0.0001$), establishing the minimum inhibitory concentration. Among six polysaccharide stabilization systems evaluated, the freeze-dried konjac glucomannan system (F-KJC) demonstrated the most consistent pH stability and lowest thermodynamic degradation (23.85% vs. 39.80% for BPFE over six freeze-thaw cycles), supported by FTIR evidence of non-covalent hydrogen bonding. Singlet oxygen quantum yield of F-KJC ($\Phi = 0.4740$) exceeded BPFE ($\Phi = 0.3014$). Under 550 nm irradiation, F-KJC significantly inhibited MRSA growth compared with non-irradiated controls, while 450 nm irradiation did not produce a statistically significant photothermal enhancement. These findings support polysaccharide stabilization, particularly the freeze-dried konjac system, as a viable strategy for enhancing the photosensitizer performance of butterfly pea anthocyanins against MRSA.

Keywords
Anthocyanin, MRSA, Photodynamic Therapy, Photothermal Therapy, Polysaccharide Stabilization

Received: 18 March 2026, Accepted: 13 June 2026
https://doi.org/10.26554/sti.2026.11.3.1192-1211

1. INTRODUCTION

Staphylococcus aureus is a major opportunistic pathogen capable of acquiring resistance to multiple antibiotic classes through diverse genetic mechanisms. Resistance has been documented against β-lactams (methicillin- resistant *S. aureus*, MRSA), glycopeptides (vancomycin-intermediate and vancomycin- resistant *S. aureus*, VISA and VRSA), linezolid (linezolid-resistant *S. aureus*, LRSA), and daptomycin, with multidrug-resistant (MDR) strains increasingly reported in both hospital and community settings (Tong et al., 2015). Among them, methicillin-resistant *Staphylococcus aureus* (MRSA) is a globally significant drug-resistant pathogen responsible for infection prevalence rates of 20–80% worldwide, causing conditions ranging from superficial skin infections to life-threatening toxic shock syndrome and pneumonia (Syahniar et al., 2020). The bacterium's expression of the *mecA*-encoded penicillin-binding protein 2a (PBP2a), which is a transpeptidase enzyme encoded by the *mecA* gene that maintains cell wall biosynthesis by operating with low affinity for β-lactam antibiotics, thereby conferring broad resistance to this antibiotic class. While prolonged reliance on vancomycin as a last-resort treatment has given rise to vancomycin-resistant *S. aureus* (VRSA), further narrowing the therapeutic arsenal (Dighriri et al., 2025).

These limitations have driven exploration of non-antibiotic approaches, among which light-based therapies, photothermal therapy (PTT) and photodynamic therapy (PDT), have emerged as promising alternatives capable of killing bacteria through localized heat generation and reactive oxygen species (ROS) production, respectively, with negligible risk of resistance development (Kong and Chen, 2022). In PTT, the photosensitizer absorbs light and converts it into localized heat

through non-radiative relaxation, raising the temperature of the target site to levels sufficient for membrane disruption and protein denaturation; in PDT, the excited photosensitizer undergoes intersystem crossing to its triplet state and transfers energy to molecular oxygen, generating cytotoxic singlet oxygen ($^1O_2$) and other reactive oxygen species that damage multiple bacterial cellular components simultaneously, as illustrated in Figure 1 (Kong and Chen, 2022; Liu et al., 2015). Despite their therapeutic promise, PTT and PDT have not yet achieved widespread clinical adoption for antibacterial applications. Key challenges include the limited tissue penetration of visible-light wavelengths, the lack of standardized photosensitizer formulations, potential phototoxicity to healthy tissue, and the absence of large-scale clinical trial data for bacterial infections specifically. Current clinical use is largely restricted to dermatological and oncological applications, with antibacterial PDT remaining predominantly at the preclinical stage (Liu et al., 2015; Overchuk et al., 2023). This study therefore contributes to the preclinical evidence base for natural photosensitizer-based PDT against drug-resistant bacteria.

A central requirement of both PTT and PDT is an effective photosensitizer. Synthetic photosensitizers such as hematoporphyrin and methylene blue have been widely studied and demonstrated efficacy against MRSA (Dai et al.; Wong et al., 2019), but their clinical translation is hampered by poor selectivity, potential heavy-metal toxicity, and high production costs Polat and Kang (2021). Natural photosensitizers derived from plants offer a compelling alternative, providing biocompatibility, biodegradability, and low environmental impact Gonçalves (2021). Among natural candidates, flavonoid-class pigments particularly anthocyanins have attracted interest due to their extended conjugated chromophore systems enabling visible-light absorption at 450–600 nm and their capacity to generate singlet oxygen through Type II photodynamic pathways Oliveira et al. (2020). Butterfly pea flower (*Clitoria ternatea* L.) is an abundant tropical source of anthocyanins (up to ~275 mg/L), dominated by polyacylated delphinidin derivatives (ternatin series) and coumaroylated glycosides, which have demonstrated intrinsic antibacterial and antibiofilm activity against staphylococci (Hamzah et al., 2024; Jeyaraj et al., 2022), and has been identified as one of the most promising natural photosensitizer candidates among plant-derived pigment sources, demonstrating significant photothermal response under 450 nm and 550 nm laser irradiation comparable to other anthocyanin-rich plant extracts Fithri et al. (2026). However, despite the established antibacterial properties of butterfly pea anthocyanins, their application as photosensitizers for PDT against MRSA has not been systematically investigated; existing related studies have focused on nanoparticle-conjugated BPF extract rather than the stabilized anthocyanin fraction as the photosensitizer itself Astuti et al. (2024), leaving a gap in direct anthocyanin-mediated photodynamic antibacterial research.

A critical barrier to the therapeutic use of anthocyanins is their instability; the flavylium cation chromophore undergoes pH-driven structural transformations and thermal degradation that diminish light-absorption capacity and ROS-generating potential Xue et al. (2024). Polysaccharide-based encapsulation systems, including chitosan, pullulan, and konjac glucomannan (KGM), have been shown to retard anthocyanin degradation through hydrogen bonding and steric encapsulation (Dong et al., 2023; Takeno et al., 2022), yet their application specifically to enhance photosensitizer performance in anti-MRSA PDT/PTT has not been reported. Furthermore, while molecular docking studies have identified several phytochemicals as PBP2a inhibitors (Gomaa et al., 2025), computational validation of *C. ternatea* anthocyanins against this key MRSA resistance target is lacking. Therefore, this research focuses on stabilization of butterfly pea anthocyanin extract using a freeze-dried konjac glucomannan system and evaluates its performance as a natural photosensitizer against MRSA. The objectives of this research are to: (1) evaluate the *in silico* binding affinity of major butterfly pea anthocyanins against the PBP2a receptor, (2) determine the minimum inhibitory concentration of the extract against *S. aureus*, (3) assess the pH and thermodynamic stability of polysaccharide-stabilized anthocyanin systems, (4) determine the singlet oxygen quantum yield of stabilized and unstabilized extract, and (5) evaluate the photothermal and photodynamic antibacterial efficacy against MRSA. The general scheme of the research can be seen in Figure 2.

2. EXPERIMENTAL SECTION

2.1 Materials

Butterfly pea flowers (*Clitoria ternatea* L.) were obtained from Palembang, South Sumatra, Indonesia, and authenticated at Herbarium ANDA, Universitas Andalas (letter no. 047/K-IDE/ANDA/I/2026) as belonging to family Fabaceae. Konjac glucomannan (KGM), maltodextrin (MDX), chitosan (CHT), and pullulan (PUL) were obtained from Subur Kimia Jaya, Ingmao, Chimultiguna, and Tritunggal Kimia. Methylene blue was used as a positive control photosensitizer. 1,3- Diphenylisobenzofuran (DPBF) was obtained from Sigma Aldrich and used as a singlet oxygen probe. Vancomycin was obtained from Xi'an Qiushi and used as the antibacterial positive control. MRSA ATCC 33591 was obtained from Thermo Scientific, while Mueller–Hinton broth (MHB) and Mueller–Hinton agar (MHA) were obtained from Merck and used for bacterial culture. All other reagents were of analytical grade.

2.2 Methods

2.2.1 Plant Material Preparation and Extraction

Butterfly pea flowers were conventionally oven-dried at 60°C and their moisture content maintained at 4% ± 2% (w/w) to minimize degradation of bioactive compounds. The dried flowers were ground and sieved through a #20 mesh screen to obtain a uniform particle size, improving solvent contact during extraction (Putra et al., 2021). Extraction was performed by macerating the simplicia (1:8 w/v) in 60% ethanol for 30 minutes at room temperature, followed by ultrasonic-assisted extraction (UAE) for 45 minutes. This condition was selected based on

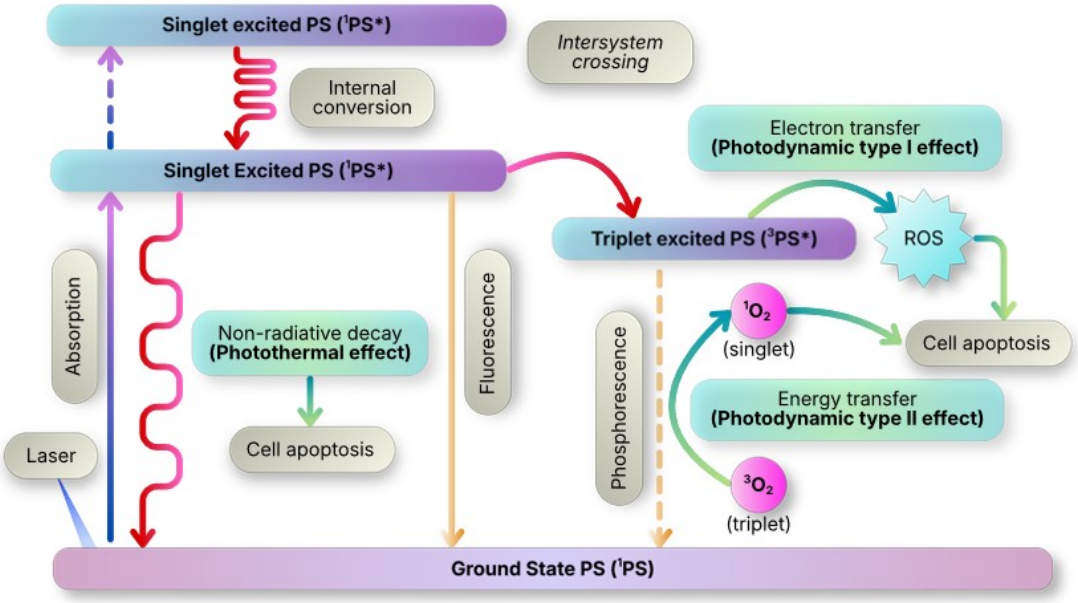

Figure 1. Jablonski's Schematic Diagram of Photothermal and Photodynamic Therapy

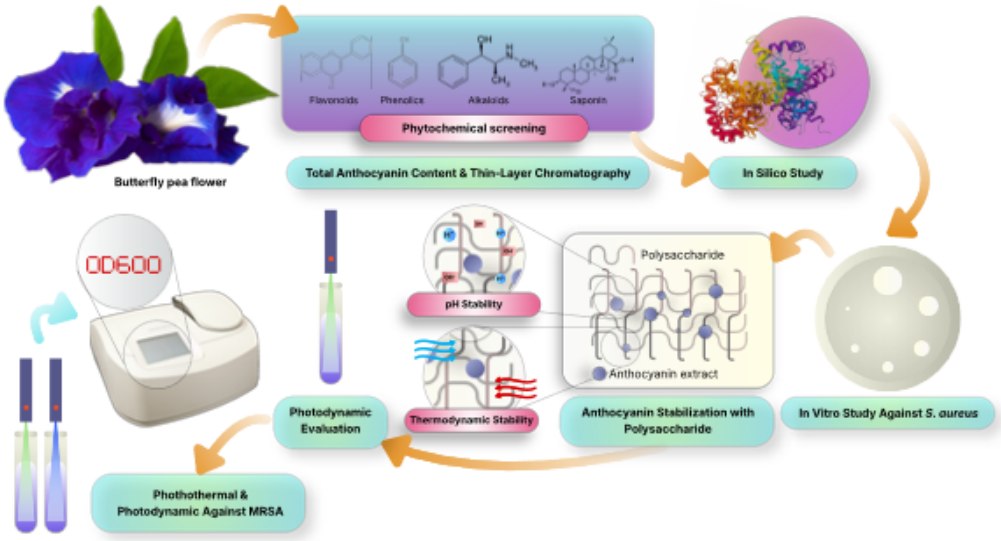

Figure 2. Schematic Overview of the Study Workflow

evaluation of multiple extraction variables including solvent concentration (40–80%), maceration time (15–45 min), and extraction method (maceration, UAE, and microwave-assisted extraction/MAE), with UAE consistently yielding higher anthocyanin content at moderate conditions (Putra et al., 2021; Thuy et al., 2021). The extract was filtered and stored at 4°C protected from light until further analysis.

2.2.2 Total Anthocyanin Content (TAC) Measurement

Total anthocyanin content (TAC) was determined using the pH differential method, which exploits the reversible structural transformation of anthocyanins between the coloured flavylium cation at pH 1.0 and the colourless carbinol pseudobase at pH 4.5 (Wrolstad et al., 2005). A working solution of 2000 ppm extract was diluted 10× with two buffer systems: (1) chloride buffer (0.025 M KCl, pH 1.00), and (2) acetate buffer (0.4 M sodium acetate, pH 4.50). Each diluted sample was equilibrated at room temperature for 15 minutes prior to measurement to ensure complete structural equilibration of the anthocyanin species at each pH.

Absorbance was measured at the wavelength of maximum absorption (λ_{max}) and at 700 nm to correct for haze and non-

anthocyanin background absorbance, using a UV–Visible spectrophotometer. The corrected absorbance (A) was calculated as Equation (1), while monomeric TAC was calculated as Equation (2).

$$A = (A_{\max} - A_{700})_{\text{pH 1.0}} - (A_{\max} - A_{700})_{\text{pH 4.5}} \quad (1)$$

$$\text{TAC (CGE/L)} = \frac{A \times MW \times DF \times 1000}{\varepsilon \times l} \quad (2)$$

Where MW is the molecular weight of the reference anthocyanin (cyanidin-3-glucoside, 449.2 g/mol), DF is the dilution factor (10), ε is the molar absorptivity of cyanidin-3-glucoside (26,900 L mol^{-1} cm^{-1}), and l is the path length of the cuvette (1 cm). Although *C. ternatea* anthocyanins are predominantly delphinidin derivatives, cyanidin-3-glucoside equivalents are used as the reference standard as it is the only commercially available anthocyanin with a universally validated molar absorptivity, established through the AOAC collaborative study across multiple laboratory matrices (Lee et al., 2005). All measurements were performed in triplicate and results reported as mean ± SD.

2.2.3 Photothermal Efficiency Measurement

Photothermal efficiency (η) was determined to evaluate the capacity of the butterfly pea anthocyanin extract to convert absorbed light energy into thermal energy. A volume of 5 mL of extract at 2000 ppm was placed in a quartz cuvette and irradiated using a 450 nm and 550 nm diode laser (0.3 W/cm^2 and 0.1 W/cm^2, 100 mm distance). Temperature was recorded every 10 seconds during a 5-minute irradiation phase (heating) and subsequently every 10 seconds during a 5-minute post-irradiation phase (cooling) using a calibrated thermometer. The temperature rise and cooling profile were used to derive the system time constant (τ_s) from the linear portion of the cooling curve. Photothermal conversion efficiency (η) was calculated according to Fithri et al. (2023) and Azzahra et al. (2025), originally developed by Roper et al. (2007) using Equation (3).

$$\eta = \frac{(T_{\max} - T_{\text{surr}})}{I\,(1 - 10^{-A})} \times mC\tau_s \quad (3)$$

Where $T_{\max}$ is the maximum temperature reached during irradiation (°C), T_{surr} is the ambient temperature prior to irradiation (°C), I is the incident laser power (W), and A is the absorbance of the extract at 450 nm or 550 nm. The heat dissipation term ($mC\tau_s$) was incorporated to account for heat loss to the surrounding environment during measurement, where m is the sample mass (g), C is the heat capacity of the solvent (J/g·°C), and τ_s is the system time constant derived from the cooling curve. The energy delivered to the sample during irradiation was calculated as Equation (4) where t is the irradiation duration in seconds. All measurements were performed in triplicate and results reported as mean ± SD.

$$E = \eta \times I \times t \quad (4)$$

2.2.4 Extract Characterization

Phytochemical screening was conducted to determine the presence of phytochemical compounds in the form of flavonoids, tannins, alkaloids, and saponins with qualitative analysis with methods following Solihah et al. (2018). Results were recorded as positive (+) or negative (–) based on the characteristic color change or precipitate formation for each respective reagent.

Flavonoids and Phenolics. One mL of extract was added to 3 mL of chloroform and boiled for 5 minutes. The mixture was allowed to stand until phase separation occurred. The aqueous phase was pipetted onto a spot plate, to which a sufficient amount of magnesium powder and 5 drops of concentrated hydrochloric acid were added. A positive result for flavonoids was indicated by the appearance of red, yellow, or orange coloration. The chloroform phase was pipetted onto a spot plate, to which 5 drops of NaOH 10% was added. A positive result for phenolics was indicated by the appearance of orange coloration.

Alkaloids. One gram of extract was added to 1 mL of 2N HCl and 9 mL of distilled water, heated for 2 minutes, cooled, and filtered. One mL of the filtrate was distributed into three separate test tubes, to which 5 drops of Mayer's reagent were added to the first tube. A positive result for alkaloids was indicated by the formation of a white precipitate in the first tube.

Steroids and Terpenoids. One mL of the chloroform phase obtained from the flavonoid test was transferred onto a spot plate, to which 5 drops of Liebermann–Burchard reagent were added. A positive result for steroids was indicated by the formation of a blue or green ring layer, while terpenoids were indicated by a red-violet coloration.

Saponins. One mL of extract was added to 10 mL of distilled water and heated for 5 minutes. The mixture was filtered and the filtrate collected, then shaken for approximately 10 seconds. One mL of 2M HCl was added to the filtrate after allowing it to stand for approximately 10 minutes. A positive result for saponins was indicated by the formation of stable foam.

TLC analysis was performed to identify the anthocyanin components present in the butterfly pea flower extract. Chromatography was conducted on silica TLC plates, which were pre-activated by heating at 110°C for 10 minutes prior to use. A volume of 2 μL of extract was spotted onto the plate using a micropipette at a distance of 1.5 cm from the lower edge, and the spot was allowed to dry completely before development. The mobile phase used was a ethyl acetate:acetic acid glacial:formic acid:aquadest (1:1:1:1, v/v/v/v) system. The chromatography chamber was saturated with mobile phase vapor for 15 minutes before plate development. The plate was developed until the solvent front reached approximately 1 cm from the upper edge of the plate, then removed and allowed to air dry (Yanti et al., 2022). Spot detection was performed under

visible light, where anthocyanin spots appear as distinctly colored bands without the need for derivatization reagents, owing to the inherent chromophore of the flavylium cation. Retardation factor (Rf) values were calculated for each resolved spot according to Equation (5).

$$Rf = \frac{\text{distance traveled by compound}}{\text{distance traveled by solvent}} \quad (5)$$

2.2.5 In Silico Molecular Docking

Three-dimensional structure of PBP2a (PDB ID: 1MWU; resolution: 2.60 Å) was retrieved from the RCSB Protein Data Bank (rcsb.org) and prepared by removing water molecules, adding polar hydrogen atoms, and computing Gasteiger charges before conversion to PDBQT format. Ligand structures were obtained from the PubChem database (pubchem.ncbi.nlm.nih.gov). All ligand and receptor preparations were performed using AutoDock Tools 1.5.7. Docking was performed using a grid box centered at the co-crystallized ligand binding site with coordinates (x = 28.221, y = 28.839, z = 87.515) and dimensions of 22×28×12 Å. The exhaustiveness was set to 32 and 10 binding poses were generated per complex. To validate the docking protocol, re-docking of the co-crystallized native ligand, (2R,4S)-2-[(1R)-1-{[(2,6-dimethoxyphenyl)carbonyl] amino}-2-oxoethyl]-5,5-dimethyl-1,3-thiazolidine-4- carboxy lic acid, was performed using identical grid box parameters (Shivanika et al., 2022). The root-mean-square deviation (RMSD) between the re-docked pose and the crystallographic conformation was calculated using PyMOL 2.5 (pymol.org); an RMSD value below 3.0 Å was considered acceptable for protocol validation. Novobiocin was included as a positive control inhibitor and cross-docked against PBP2a using identical grid box parameters and docking settings to provide a binding affinity benchmark for comparison with the screened compounds.

Prior to docking, thirty-six compounds of butterfly pea flower (*Clitoria ternatea*) identified from the KNApSAcK database (knapsackfamily.com/KNApSAcK/) were subjected to a two-stage screening workflow. In the first stage, biological activity prediction was performed using PASS Online (way2drug.com/passonline), in which charged compounds were converted into their neutral forms. Compounds were evaluated for antibacterial activity, cell wall synthesis inhibition, topoisomerase inhibition, and membrane integrity disruption; compounds were retained if they demonstrated a probability of activity (Pa) exceeding 0.30 for at least one target activity. In the second stage, pharmacokinetic and toxicity profiling was performed using Deep-PK (https://biosig.lab.uq.edu.au/deeppk/). Compounds were scored based on molecular weight (≤ 650 Da), lipophilicity (LogP: −2 to 6), aqueous solubility (LogS > −4), topological polar surface area (TPSA ≤ 180 Å^2), hydrogen bond donors (≤ 5), hydrogen bond acceptors (≤ 10), rotatable bonds (≤ 10), AMES mutagenicity (non-mutagenic), hERG channel inhibition (non-inhibitor), hepatotoxicity (non-hepatotoxic), and skin sensitization (non-sensitizer). A composite scoring system with a maximum of 17 points was applied, and compounds scoring ≥ 9 were retained. Eighteen compounds meeting these criteria were selected for molecular docking.

All 18 screened compounds were docked against PBP2a. From the resulting binding affinities, the three compounds exhibiting the lowest (most negative) binding affinity values were selected for detailed interaction analysis. Binding interactions including hydrogen bonding (H-bond distance ≤ 3.0 Å) and amino acid residues were visualized using PyMOL 2.5 and Discovery Studio 2025 (Edityaningrum et al., 2026; Ramadhani et al., 2024).

2.2.6 Antibacterial Activity

Antibacterial activity against *Staphylococcus aureus* (SA) was assessed using the disc diffusion method on Mueller–Hinton agar. Extract concentrations of 2%, 4%, 6%, and 8% (w/v) were tested with vancomycin 0.1% as positive control and sterile distilled water as negative control. Plates were incubated at 37°C for 20 hours and inhibition zones measured in triplicate. The minimum inhibitory concentration (MIC) was determined as the lowest concentration producing a statistically significant inhibition zone compared with lower concentrations.

2.2.7 Stabilization Systems and Evaluation

Four polysaccharide systems were prepared in the ratio of 0.1:2 (w/w) in maltodextrin (MDX), chitosan (CHT), pullulan (PUL), and konjac glucomannan (KJC) in both gel (KJC) and freeze-dried (F-KJC) forms, along with freeze-dried maltodextrin (F-MDX). All systems were formulated using the MIC concentration (8%) of BPFE. F-KJC was prepared by freeze-drying the KJC gel using standard lyophilization conditions. pH stability was assessed by measuring absorbance at approximately 627 nm (the maximum wavelength of butterfly pea anthocyanin extract at pH 3.20) in buffer solutions at pH 1.20, 4.50, 6.80, 7.40, 7.48, and 9.00 after 24 hours incubation at room temperature. Thermodynamic stability was assessed by subjecting systems to six freeze-thaw cycles and measuring absorbance at cycle 1 and cycle 6, with percent decrease calculated as a stability index.

2.2.8 Singlet Oxygen Quantum Yield

Singlet oxygen generation was evaluated using the DPBF photodegradation method. Samples (BPFE and F-KJC, 1000 ppm each) and controls (methylene blue 1 ppm as positive; 60% ethanol as negative) were irradiated using a 550 nm diode laser (0.1 W/cm^2) in a dark chamber. Absorbance at 410 nm was recorded every 60 seconds for 9 minutes. A parallel experiment was conducted under ambient light to distinguish photodynamic activity from photo-oxidation. The first-order reaction rate constant (K) was calculated from the slope of $\ln(A_0/A)$ versus time as seen in Equation (7). The quantum yield (Φ) was calculated relative to methylene blue using the comparative method as seen in Equation (6), while the F factor can be calculated with Equation (8) (Bresolí-Obach et al.,

Table 1. Molecular Docking Binding Affinities against PBP2a Receptor

Compound	Binding Affinity (kcal/mol)
Novobiocin (positive control)	-11.2
Preternatin C4	-11.1
Kaempferol 3-O-robinobioside	-11.0
Kaempferol 3-rutinoside	-11.0
Clitorin	-10.9
Astragalin	-10.7
Kaempferol 3-neohesperidoside	-10.7
Myrtillin	-10.5
Hirsutrin	-10.4
Cyanin	-10.0
Delphin	-9.9
Manghaslin	-9.8
Petunidin 3-glucoside	-9.8
Oenin	-9.7
Delphinidin chloride	-9.1
Genistein	-8.5
Kaempferol 3-(6G-malonylneohesperidoside)	-7.6
Delphinidin 3-(2-rhamnosyl-6-malonylglucoside)	-7.4
Quercetin 3-(6”-malonylneohesperidoside)	-7.4

2021).

$$\phi_{\Delta}^{\text{sample}} = \phi_{\Delta}^{\text{baku}} \times \frac{k_{\text{sample}}}{k_{\text{baku}}} \times \frac{F_{\text{baku}}}{F_{\text{sample}}} \quad (6)$$

$$k = -\frac{dA}{dt} \quad (7)$$

$$F = 1 - 10^{-A_{\lambda}} \quad (8)$$

2.2.9 Photothermal and Photodynamic Antibacterial Activity

MRSA growth was first characterized to identify mid-logarithmic phase (12–14 hours). Antibacterial testing used the optical density (OD) method at 600 nm, measuring turbidity changes over 24 hours. Two laser wavelengths were applied: 450 nm (blue, 0.3 W/cm^2) for photothermal testing and 550 nm (green, 0.1 W/cm^2) for photodynamic testing, consistent with anthocyanin absorption. Tested groups were BPFE, F-KJC, positive control (vancomycin 0.1%), and negative control (broth only), each with and without laser irradiation (Fithri et al., 2025).

2.2.10 Statistical Analysis

Data are presented as mean ± SD. Prior to analysis, normality was assessed using the Shapiro–Wilk test and homogeneity of variance using Levene’s test. When assumptions were satisfied, differences among groups were analyzed by one-way ANOVA followed by Tukey’s post-hoc test or Dunnett’s multiple comparisons test where appropriate, conducted in GraphPad® Prism 10. Significance was defined as (*) $p < 0.05$, (**) $p < 0.01$, (***) $p < 0.001$, and (****) $p < 0.0001$. FTIR spectra were analyzed using Origin® 2026, and docking results were interpreted by binding affinity (kcal/mol) and amino acid residue.

3. RESULTS AND DISCUSSION

3.1 Total Anthocyanin Content (TAC)

Total anthocyanin content (TAC) of butterfly pea extract was determined in triplicate for both dried and fresh flower simplicia using the pH differential method (Wrolstad et al., 2005). As seen in Figure 3a, dried flower extract yielded a mean TAC of 5.037 ± 0.395 mg CGE/L, while fresh flower extract yielded a notably lower mean TAC of 2.415 ± 0.532 mg CGE/L. Dried flowers produced approximately 2.08-fold higher TAC compared to fresh flowers, and the substantially lower CV of the dried extract indicates superior measurement reproducibility. The CV of the dried extract (7.85%) was lower than that of fresh extract (22.03%), suggesting more consistent extraction yields from the dried simplicia, though both values are somewhat higher than the inter-laboratory RSD of 1.06–4.16% reported for the AOAC pH differential protocol (Lee et al., 2005), likely reflecting the complexity of the *C. ternatea* anthocyanin profile relative to the fruit juice matrices used in the original collaborative study.

The higher TAC in dried flower extract is attributable to the concentration effect of moisture removal during oven drying at 60°C to 4% ± 2% moisture content. Drying reduces free water content, concentrating the anthocyanin fraction per unit mass and reducing aqueous dilution during solvent extraction. Additionally, controlled low-temperature drying may also disrupt

cell wall structures, potentially improving solvent penetration and anthocyanin accessibility (Khoo et al., 2017). The higher CV observed in fresh flower extracts reflects the inherent variability of fresh plant material; differences in individual flower maturity, turgor pressure, and water content between replicates may produce less consistent extraction yields compared to the homogenized, standardized dried simplicia (Handayani et al., 2024). These observations support dried simplicia as a more reproducible starting material for anthocyanin extraction.

The TAC of dried extract (5.037 mg CGE/L) is consistent with literature values for moderate-concentration aqueous ethanol extracts of *C. ternatea*. Jeyaraj et al. (2022) reported a TAC of 5.1 mg CGE/g dry weight using 50% ethanol, suggesting that moderate aqueous ethanol concentrations may be sufficient for monomeric anthocyanin recovery. Thuy et al. (2021) reported a higher TAC of 39.90 mg/L using UAE at 74°C for 56.88 minutes, substantially exceeding the present study's value, which is expected given the elevated temperature and extended extraction time promoting greater anthocyanin solubilization. The lower TAC in this study is consistent with extraction at room temperature with a short maceration time of 30 minutes, which are less aggressive conditions likely yielding lower absolute anthocyanin content. A study by Ikhwanurridlo et al. (2025) confirmed that UAE enhances anthocyanin yield by approximately 90% relative to crude powder, and the 45-minute UAE step incorporated after maceration in this protocol is consistent with this enhancement principle. Since degraded or polymeric anthocyanin species do not contribute to photosensitizing activity, preservation of monomeric integrity takes precedence over maximizing absolute yield (Wrolstad et al., 2005). The dried flower extract TAC of 5.037 mg CGE/L therefore reflects a functionally relevant, structurally intact anthocyanin fraction, and dried simplicia was selected as the starting material for all subsequent stabilization and photodynamic evaluations.

3.2 Photothermal Efficiency

Photothermal efficiency (η) was measured as a preliminary characterization of the extract's light-to-heat conversion capacity, providing a quantitative basis for evaluating the extract's potential as a PTT agent prior to antibacterial testing. Photothermal efficiency (η) was measured under two laser wavelengths selected based on the absorption characteristics of butterfly pea anthocyanins. The flavylium cation form of delphinidin-based anthocyanins, which predominates at the native extract pH (~3.2), exhibits two principal absorption bands: a high-energy B-band at approximately 450 nm arising from aromatic π–π^* transitions of the acylated chromophore, and a primary Q-band at approximately 550–630 nm corresponding to the visible charge-transfer transition of the flavylium system responsible for the characteristic blue-purple colour (Dong et al., 2024). These two bands represent the wavelengths at which butterfly pea anthocyanin most efficiently harvests photons and were therefore selected as the excitation wavelengths for characterizing the photophysical properties of this extract. The 450 nm wavelength was selected to characterize photothermal conversion efficiency since the π–π^* transition at this wavelength channels absorbed energy primarily into vibrational relaxation and internal conversion, heat-generating non-radiative pathways, rather than into the intersystem crossing that produces singlet oxygen. Conversely, the 550 nm wavelength aligns with the Q-band transition that has been reported to promote intersystem crossing from S_1 to T_1, making it the more appropriate excitation source for photodynamic ROS generation and quantum yield measurement (Oliveira et al., 2020). The use of two wavelengths therefore reflects the mechanistic duality of anthocyanin's photophysical behaviour: 450 nm was used to probe photothermal capacity and 550 nm was used to probe photodynamic capacity, consistent with the combined PTT/PDT therapeutic strategy of this study.

It is acknowledged that both wavelengths fall within the visible light range (450–630 nm) rather than the near-infrared (NIR) therapeutic window (700–1100 nm) conventionally preferred for biomedical photothermal applications due to deeper tissue penetration and lower phototoxicity to intervening tissue (Ziesmer et al., 2023). The use of visible wavelengths in this study is constrained by the intrinsic absorption profile of anthocyanins, which do not absorb meaningfully in the NIR region without chemical modification or nanoparticle conjugation. As such, the photothermal and photodynamic evaluations presented here are intended as *in vitro* proof-of-concept characterizations of the extract's photophysical properties, and direct extrapolation to *in vivo* or deep-tissue therapeutic applications would require further investigation, including nanoformulation strategies to red-shift the absorption profile toward the NIR window (Astuti et al., 2024).

Under 450 nm irradiation (0.3 W/cm^2), the mean photothermal efficiency was 52.34 ± 7.93%, while in 550 nm irradiation (0.1 W/cm^2), the mean efficiency was considerably lower at 22.21 ± 2.35% as seen in Figure 3b. Although these values are not directly comparable to NIR-active photothermal agents, which typically achieve efficiencies of 40–80% under 808 nm irradiation (Ziesmer et al., 2023), the photothermal efficiency of 52.34% at 450 nm is notable for an unmodified natural extract and supports its potential for surface-level or *in vitro* antibacterial applications where tissue penetration depth is not a limiting factor. The difference in efficiency between wavelengths might be attributable to the stronger π–π^* absorption cross-section of the acylated delphinidin chromophore at 450 nm compared to 550 nm, in addition to the higher laser power applied at 450 nm (0.3 W/cm^2 vs. 0.1 W/cm^2), which confounds direct mechanistic comparison between the two wavelengths.

3.3 Extract Characterization

The phytochemical screening showed that *C. ternatea* contained flavonoids, phenolics, alkaloids, and saponins (Figure 4b–e). Flavonoids were confirmed positive by the appearance of orange coloration, while phenolics were confirmed positive by the appearance of orange coloration, indicative of the presence of

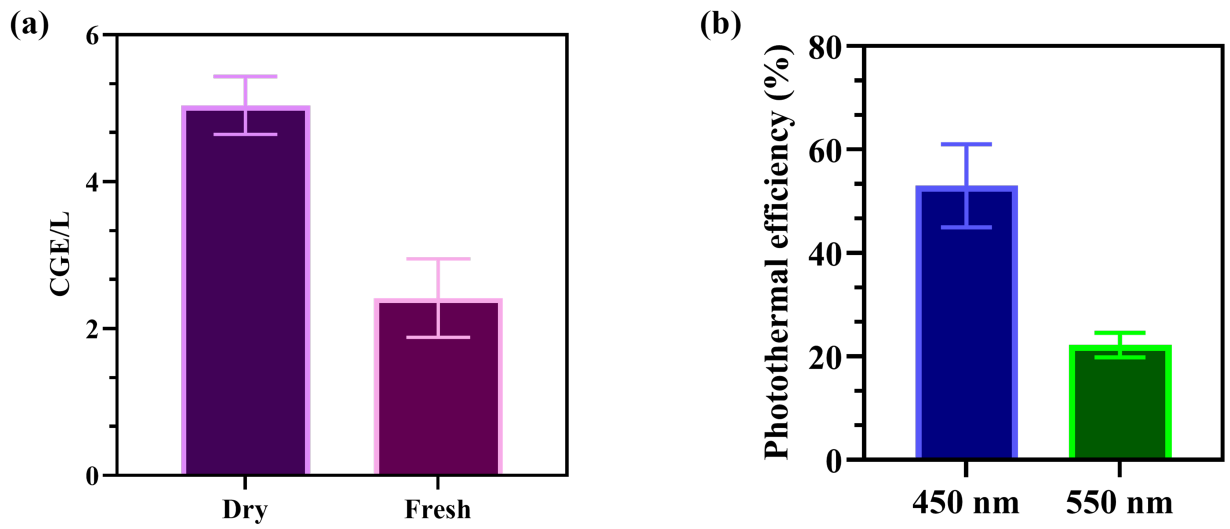

Figure 3. Total Anthocyanin Content of (a) Dry and Fresh Flower, and (b) Photothermal Efficiency in 450 and 550 nm

hydroxyl-bearing aromatic compounds; the positive phenolic response is consistent with the known abundance of polyhydroxylated flavonoids and anthocyanins in *C. ternatea* flowers. Alkaloids were confirmed positive by the formation of a white precipitate with Mayer's reagent, indicative of the presence of nitrogenous heterocyclic compounds. Steroids and terpenoids yielded negative results in the Liebermann–Burchard test, consistent with the preferential solubilization of polar compounds by the 60% aqueous ethanol extraction system; the non-polar sterol and terpenoid fraction of *C. ternatea*, including palmitic acid, phytosterols, and tocopherols, requires non-polar solvents such as hexane or ethyl acetate for efficient extraction (Shen et al., 2016). Saponins were confirmed positive, as stable foam formation was observed following acidification of the heated aqueous filtrate. The overall phytochemical profile is consistent with previously reported screening results for *C. ternatea* flower extracts obtained with polar solvent systems (Oguis et al., 2019).

TLC analysis on silica plates with ethyl acetate:glacial acetic acid:formic acid:distilled water (1:1:1:1, v/v/v/v) mobile phase resolved three distinct spots under visible light (Yanti et al., 2022). The spot at Rf 0.45 appeared blue-cyan, tentatively consistent with delphinidin-3-glucoside, a monoglucosylated delphinidin with high polarity attributable to its free hydroxyl groups and single sugar moiety, resulting in relatively slow migration in this solvent system. The spot at Rf 0.51 appeared blue-grey, tentatively consistent with cyanidin-3-O-glucoside, which differs from delphinidin-3-glucoside by the absence of one B-ring hydroxyl group, conferring marginally greater hydrophobicity and correspondingly higher Rf (Alappat and Alappat, 2020). The spot at Rf 0.60 appeared violet, tentatively consistent with ternatin derivatives, the polyacylated delphinidin triglucosides characteristic of *C. ternatea*, whose multiple *p*-coumaroyl acyl substituents substantially increase molecular hydrophobicity relative to simple monoglucosides, driving faster migration despite their larger molecular mass (Purnamayanti et al., 2022). The violet coloration of the Rf 0.60 spot, distinct from the blue hues of the lower-Rf spots, may be indicative of intramolecular copigmentation effects associated with polyacylated anthocyanins, though definitive structural assignment would require further spectroscopic confirmation. The observed Rf values and colorations are in general agreement with reference data reported for *C. ternatea* anthocyanins under comparable TLC conditions (Arsyad et al., 2025). TLC results are shown in Figure 4a.

3.4 In Silico Molecular Docking Against PBP2a

Molecular docking was performed to provide computational evidence for the antibacterial mechanism of butterfly pea anthocyanins against MRSA. MRSA resistance is primarily mediated by the *mecA*-encoded PBP2a protein, which maintains cell wall biosynthesis in the presence of β-lactam antibiotics through its low affinity for the antibiotic binding site (Liu et al., 2015). Targeting PBP2a is therefore a validated strategy for anti-MRSA drug discovery (Gomaa et al., 2025).

Of the 18 compounds screened, all demonstrated binding affinities ranging from −7.4 to −11.1 kcal/mol against PBP2a, with 16 out of 18 (88.9%) surpassing the native ligand (−6.8 kcal/mol), and the top three compounds achieving affinities comparable to the positive control novobiocin (−11.2 kcal/mol) within AutoDock Vina's reported precision range of ±0.5 kcal/mol. These results suggest that *C. ternatea* secondary metabolites as a class may exhibit strong affinity for the PBP2a binding site, which is consistent with the polyhydroxylated aromatic structures of flavonoids and anthocyanins that provide multiple hydrogen bond donors and acceptors for receptor interaction (Gomaa et al., 2025). Full binding affinity data for all 18 compounds are presented in Table 1. The three

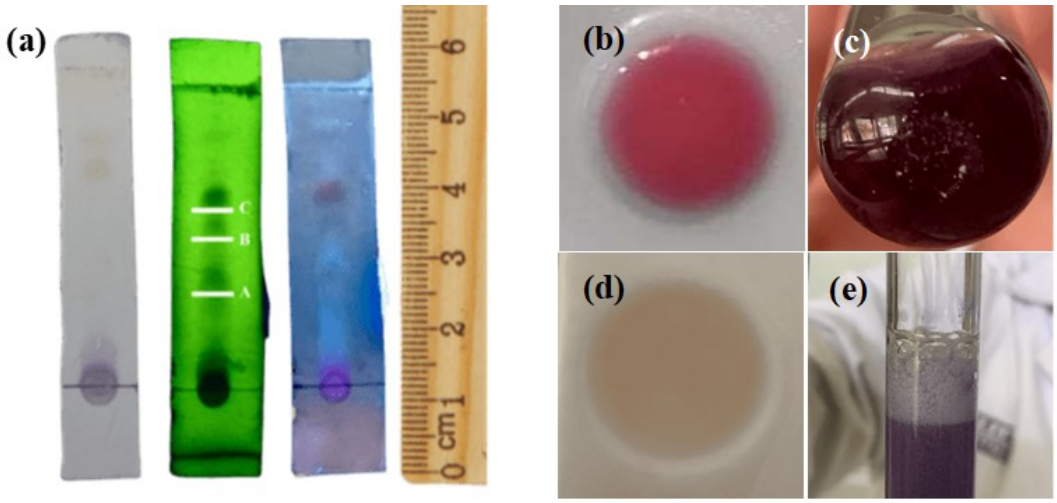

Figure 4. Result of (a) Thin-Layer Chromatography and Phytochemical Screening Results of (b) Flavonoids, (c) Phenolics, (d) Alkaloids, and (e) Saponin

compounds with the strongest binding affinities-preternatin C4 (−11.1 kcal/mol), kaempferol 3-*O*-robinobioside (−11.0 kcal/mol), and kaempferol 3-rutinoside (−11.0 kcal/mol)-were selected for detailed binding interaction analysis alongside novobiocin as a positive control reference. Their docking poses within the PBP2a active site are shown in Figure 5 and the contributing amino acid residues are summarized in Table 2.

The binding interaction analysis revealed that all three top-ranked compounds form contacts with key residues within the PBP2a active site that have been reported to be critical for its catalytic function. The active site of PBP2a is characterized by a narrow, closed allosteric cavity and a transpeptidase active site containing a catalytic triad involving SER-403, with additional contributions from residues including ASN-464, GLN-521, THR-600, LYS-406, SER-462, TYR-519, and THR-444 (Fishovits et al., 2014). Novobiocin, docked as the positive control, yielded a binding affinity of −11.2 kcal/mol and formed hydrogen bond interactions at THR-600, ASN-464, and SER-403, engaging both the allosteric and catalytic regions of PBP2a, consistent with its reported mechanism as an allosteric inhibitor that propagates conformational changes impeding acylation (Otero et al., 2013). This interaction profile provides a structural benchmark against which the screened compounds can be evaluated.

Preternatin C4, despite achieving a binding affinity comparable to novobiocin (−11.1 kcal/mol, difference of 0.1 kcal/mol within AutoDock Vina's reported precision range of ±0.5 kcal/mol), demonstrated a partially overlapping but distinct interaction profile. Preternatin C4 shared interactions at THR-600 and ASN-464 with novobiocin, suggesting engagement within the same allosteric binding region. However, Preternatin C4 additionally engaged TYR-519 and THR-444, residues not contacted by novobiocin in this study, while notably lacking direct interaction with SER-403. The engagement of TYR-519 is consistent with the polyacylated scaffold of preternatin C4, which presents extended acyl arms capable of aromatic stacking with tyrosine residues; this additional interaction may partially compensate for the absence of SER-403 contact relative to

Table 2. Amino Acid Residues

Compound	Amino Acid Residues	Distance(s) (Å)
Novobiocin	THR-600	2.8; 3.0
	ASN-464	3.0; 3.4
	SER-403	2.7; 3.5
Preternatin C4	THR-600	2.5
	ASN-464	2.8
	TYR-519	3.0
	THR-444	3.5
Kaempferol 3-O- robinobioside	GLN-521	2.3
	LYS-406	3.4
	SER-462	3.0
	SER-403	2.8; 3.4
	ASN-464	2.5; 3.4; 3.5
Kaempferol 3-rutinoside	ASN-464	3.5
	GLN-521	2.2; 2.8
	THR-600	2.8
	SER-403	2.7; 3.3; 3.5
	LYS-406	3.4
	SER-462	2.2; 2.6; 3.0

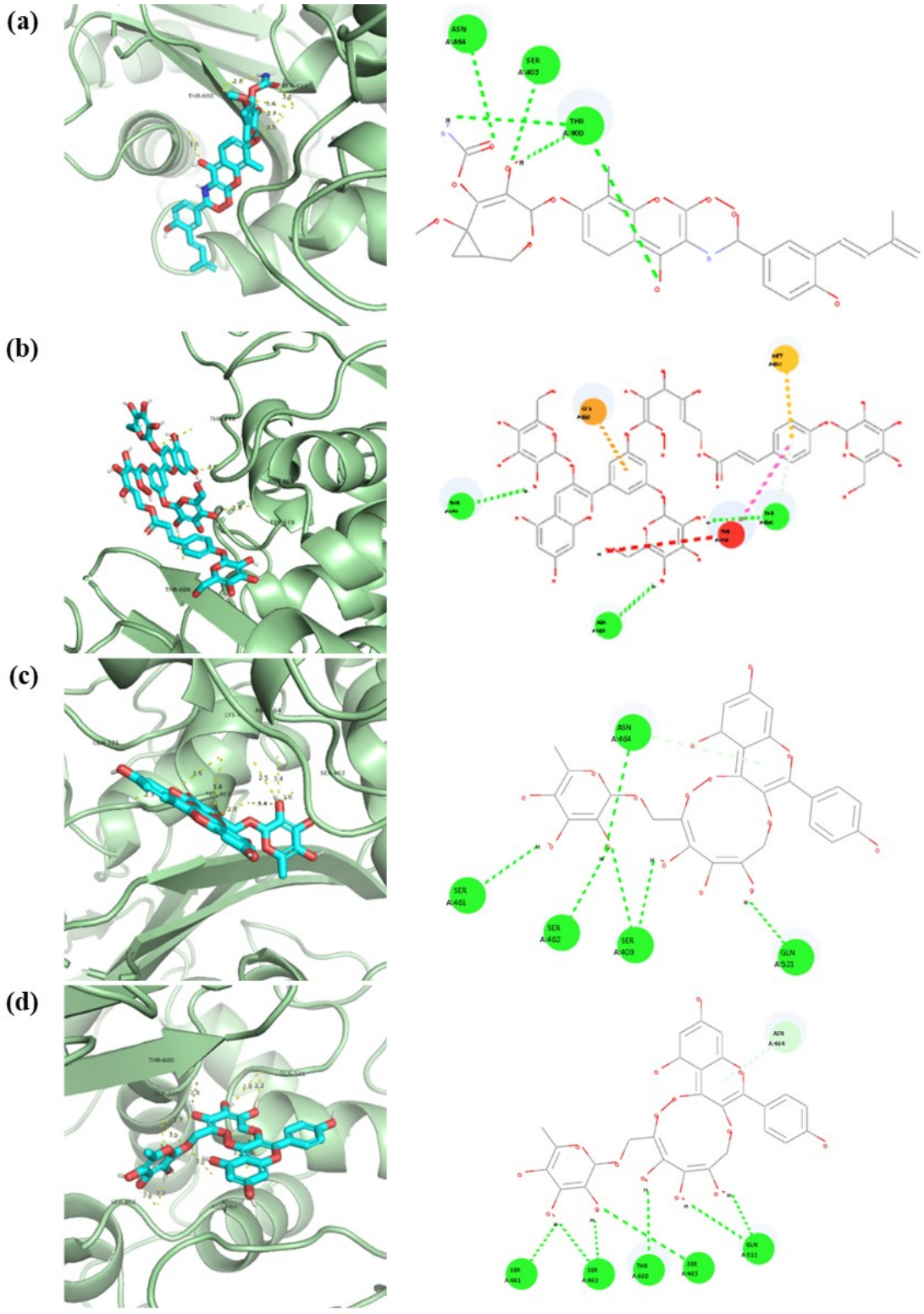

Figure 5. Visualization of Docking Poses of (a) Novobiocin, (b) Preternatin C4, (c) Kaempferol 3-O-Robinobioside, and (d) Kaempferol 3-Rutinoside Within the PBP2a Active Site Along with its Interaction Map

novobiocin. THR-600 is located within the transpeptidase domain and has been identified as a key interaction partner for allosteric PBP2a inhibitors, where binding at this region has been reported to propagate conformational changes that close the active site and impair acylation efficiency (Otero et al., 2013); its shared engagement by both preternatin C4 and novobiocin suggests a mechanistically relevant binding locus.

Kaempferol 3-*O*-robinobioside and kaempferol 3-rutinoside share a highly similar interaction profile with each other, and both demonstrate greater residue overlap with novobiocin than preternatin C4. Both compounds contacted SER-403, ASN-464, GLN-521, THR-600, LYS-406, and SER-462, with kaempferol 3-rutinoside additionally contacting THR-600, mirroring one of novobiocin's key interactions. SER-403 is part of the conserved Ser-X-X-Lys motif of class B PBPs and constitutes the nucleophilic serine responsible for β-lactam acylation; both kaempferol compounds contacted this residue with multiple hydrogen bonds, kaempferol 3-rutinoside at 2.7, 3.3, and 3.5 Å, and kaempferol 3-*O*-robinobioside at 2.8 and 3.4 Å, compared to novobiocin's single interaction at SER-403 (2.7 Å). This denser hydrogen bonding at SER-403 for the kaempferol compounds, facilitated by the multiple hydroxyl donors of their rutinosyl and robinobiosyl sugar moieties, may account for their comparable binding affinities (−11.0 kcal/mol) despite lacking the extended hydrophobic surface of preternatin C4. *In silico* binding at SER-403 suggests a potential for interference with the acylation step of cell wall transpeptidation, though this requires experimental validation (Fishovits et al., 2014). GLN-521 interactions at 2.2–2.8 Å across both kaempferol compounds fall within the range typically associated with strong hydrogen bonds (Bissantz et al., 2010) and may contribute to binding stability, though the relative contribution of individual residues cannot be determined from docking data alone.

Collectively, the convergence of interactions at THR-600 and ASN-464 across all three top compounds and novobiocin suggests engagement within a shared allosteric binding region of PBP2a. The additional contacts formed by each screened compound beyond novobiocin's interaction footprint, particularly TYR-519 for preternatin C4 and the denser SER-403 hydrogen bonding network for the kaempferol compounds, may contribute to their comparable or superior binding affinities relative to the positive control. These *in silico* findings support the hypothesis that *C. ternatea* glycosylated flavonoid and polyacylated delphinidin derivatives warrant further investigation as potential PBP2a-targeting antibacterial candidates, though experimental confirmation of inhibitory activity is required to substantiate these computational predictions.

3.5 Minimum Inhibitory Concentration against *Staphylococcus aureus*

The growth curve of *S. aureus* exhibited a lag phase (2–6 h), transition to exponential growth (6–12 h), a clear log phase (12–14 h), and stationary phase (14–24 h). The absence of an observable death phase is attributable to the turbidimetric measurement method, which records absorbance rather than cell viability; the curve therefore appears stagnant beyond 24 h even as cell death occurs (Navarro-Pérez et al., 2022). Based on this growth profile, the mid-log phase (12–14 h) was identified as the optimal inoculum standardization window, as bacteria in the lag phase may exhibit altered physiological states that affect antimicrobial susceptibility responses.

Disc diffusion results showed concentration-dependent inhibition zones across all tested concentrations. The highest inhibition zone diameter was recorded at 8% extract (10.67±0.94 mm), followed by 6% (4.00 mm), 4% (3.17 mm), and 2% (2.43 mm). One-way ANOVA with Dunnett's multiple comparisons confirmed that the 8% concentration was significantly different from all lower concentrations ($p < 0.0001$), while no significant differences were observed among the 2%, 4%, and 6% groups, suggesting that a threshold concentration effect may exist below which increasing extract dose does not produce a proportionally greater inhibitory response. This pattern has been observed in other anthocyanin-containing plant extracts and may reflect concentration-dependent interactions with bacterial membrane components, though the precise mechanism cannot be determined from disc diffusion data alone (Dong et al., 2022). Accordingly, 8% was designated as the minimum inhibitory concentration (MIC) and used in all subsequent stabilization and photosensitizer experiments.

No inhibition zone was observed for the negative control, confirming the absence of solvent-mediated inhibition. Vancomycin 0.1% produced the largest inhibition zone (24.33 mm), serving as a well-characterized positive control for antibacterial activity assessment (Dighriri et al., 2025). The coefficient of variation across all treatment replicates was below 11%, indicating acceptable measurement consistency and good assay reproducibility. The inhibition zone of 10.67 mm produced by the 8% extract is broadly comparable to values reported for other polar solvent extracts of *C. ternatea* tested against staphylococci. Ternatin B2, D1, and D2 have been identified as key bioactive components of *C. ternatea* with anti-staphylococcal activity, attributed to their ability to disrupt cell membrane integrity and interfere with cell wall synthesis (Jeyaraj et al., 2022). Additionally, *C. ternatea* extract has been reported to reduce MRSA biofilm formation, with FTIR spectral shifts in lipid, polysaccharide, and protein bands suggesting perturbation of the extracellular polymeric substance matrix (Hamzah et al., 2024). These reported mechanisms are consistent with the PBP2a binding interactions observed in the molecular docking analysis of this study, and together suggest that butterfly pea anthocyanins may act through multiple antibacterial pathways, though experimental mechanistic confirmation remains to be established. Figure 6 presents the inhibition zone data.

3.6 Anthocyanin Stabilization

Polysaccharide-based encapsulation of plant extracts has been explored for antibacterial applications, where chitosan-alginate submicro particles loaded with *Senna alata* extract were shown to improve antibacterial performance against *P. acne* relative to

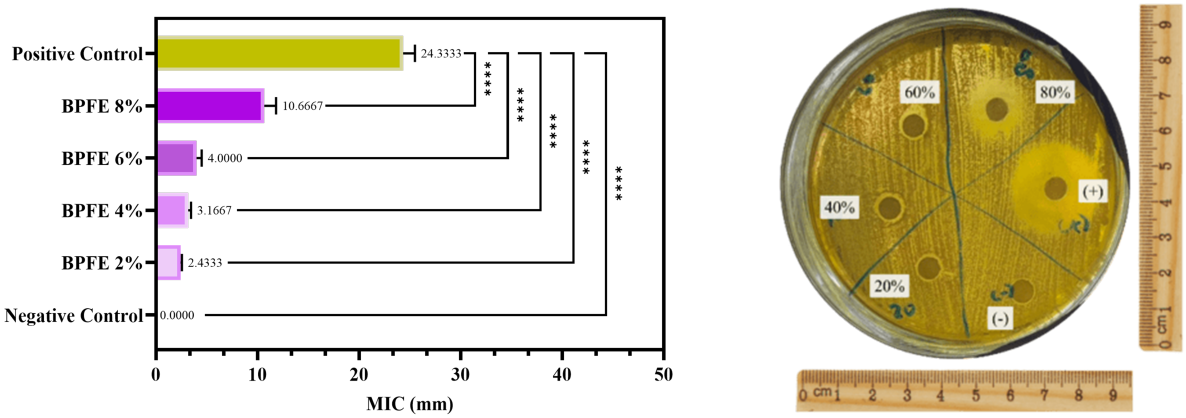

Figure 6. Inhibition Zone Diameters of Butterfly Pea Extract against *Staphylococcus aureus* ($^{*}p$ <0.0001)

the crude extract (Mardiyanto et al., 2020). Two polysaccharide-based approaches were evaluated for anthocyanin stabilization: gel systems (maltodextrin/MDX, chitosan/CHT, pullulan/PUL, and konjac glucomannan/KJC) and freeze-dried systems (freeze-dried maltodextrin/F-MDX and freeze-dried konjac glucomannan/F-KJC). Each polysaccharide was selected on the basis of its distinct structural properties. MDX was chosen for its amorphous glucose chain structure, which forms hydrogen bonds with the polar flavylium cation, creating a protective matrix that reduces direct anthocyanin contact with oxygen and light, a mechanism reported to improve anthocyanin retention by up to 30% (Ozcelik and Kulozik, 2023). CHT stabilizes anthocyanin through electrostatic interactions and hydrogen bonding via its protonatable primary amine groups ($-NH_2$), which increase thermal decomposition temperature and reduce moisture permeability (Li and Li, 2025). PUL provides protection through its linear α-(1→6)-glucan chain network, which forms a dense, homogeneous film that restricts oxygen and water diffusion into the matrix (Kraśniewska et al., 2017). KJC was selected for its glucose–mannose copolymer backbone, whose abundant hydroxyl groups enable formation of a three-dimensional hydrogen-bonded gel network that physically entraps anthocyanin molecules and limits their mobility (Takeno et al., 2022).

pH stability was assessed by monitoring normalized absorbance at ~627 nm, the anthocyanin λ_{max} at the native extract pH of 3.20, across six buffer conditions (pH 1.2, 4.5, 6.8, 7.4, 7.4 PBS, and 9.0) after 24 hours of incubation. As shown in Figure 7a, the normalized absorbance of all systems declined as pH increased from acidic to basic conditions, consistent with the well-established structural transformations of anthocyanins at higher pH: at pH 1.2 the red flavylium cation predominates; at pH 4–5 the colourless carbinol pseudobase forms; at pH 6–7 the blue quinoidal base appears; and beyond pH 7 the yellow chalcone structure accumulates, all of which absorb differently at 627 nm (Xue et al., 2024). BPFE and several gel systems (MDX, CHT, PUL) showed sharper absorbance declines particularly near neutral to alkaline pH, reflecting their limited protection against pH-driven structural transformation. F-KJC demonstrated the most consistent absorbance profile across all six pH conditions, with the smallest fluctuation range from acidic to basic pH compared to all other systems. Notably, KJC gel maintained the highest absolute absorbance values across conditions, while F-KJC showed lower absolute absorbance but superior consistency. The higher absolute absorbance of KJC gel may be partly attributable to the light-scattering characteristics of the hydrated gel matrix itself, which artificially elevates measured absorbance relative to the true chromophore concentration. While its mechanism as stabilizer for anthocyanin might be contributed by its ability to delay diffusion of ions or heat (Takeno et al., 2022), as illustrated in Figure 7c. F-KJC, following lyophilization and redispersion, loses this scattering contribution, making its absorbance readings a more accurate reflection of true anthocyanin stability. The uniformity of F-KJC's response across pH conditions indicates that the freeze-dried konjac matrix forms a homogeneous solid protective environment that buffers anthocyanin against pH-driven structural changes, likely through the same tortuous pathway mechanism that restricts hydrolysis and oxidation reactions (Yang et al., 2017), as illustrated in Figure 7d. ANOVA with Tukey's multiple comparisons confirmed significant differences between F-KJC and most other systems at multiple pH conditions ($p < 0.0001$). The spectrophotometric behavior of butterfly pea anthocyanins under storage conditions, including degradation kinetics of the flavylium cation and acyl groups, has been characterized by first-order reaction models (Marpaung and Pustikarini, 2023), providing a mechanistic basis for the pH-driven absorbance changes observed in the present study.

Thermodynamic cycling stability was evaluated over six alternating cycles of 25 °C and −25 °C storage (24 h each), simulating repeated freeze-thaw stress. Absorbance was recorded at cycle 1 and cycle 6 for all systems, and the percentage absorbance decline was calculated. As shown in Figure 7b, all systems experienced measurable absorbance decline after six

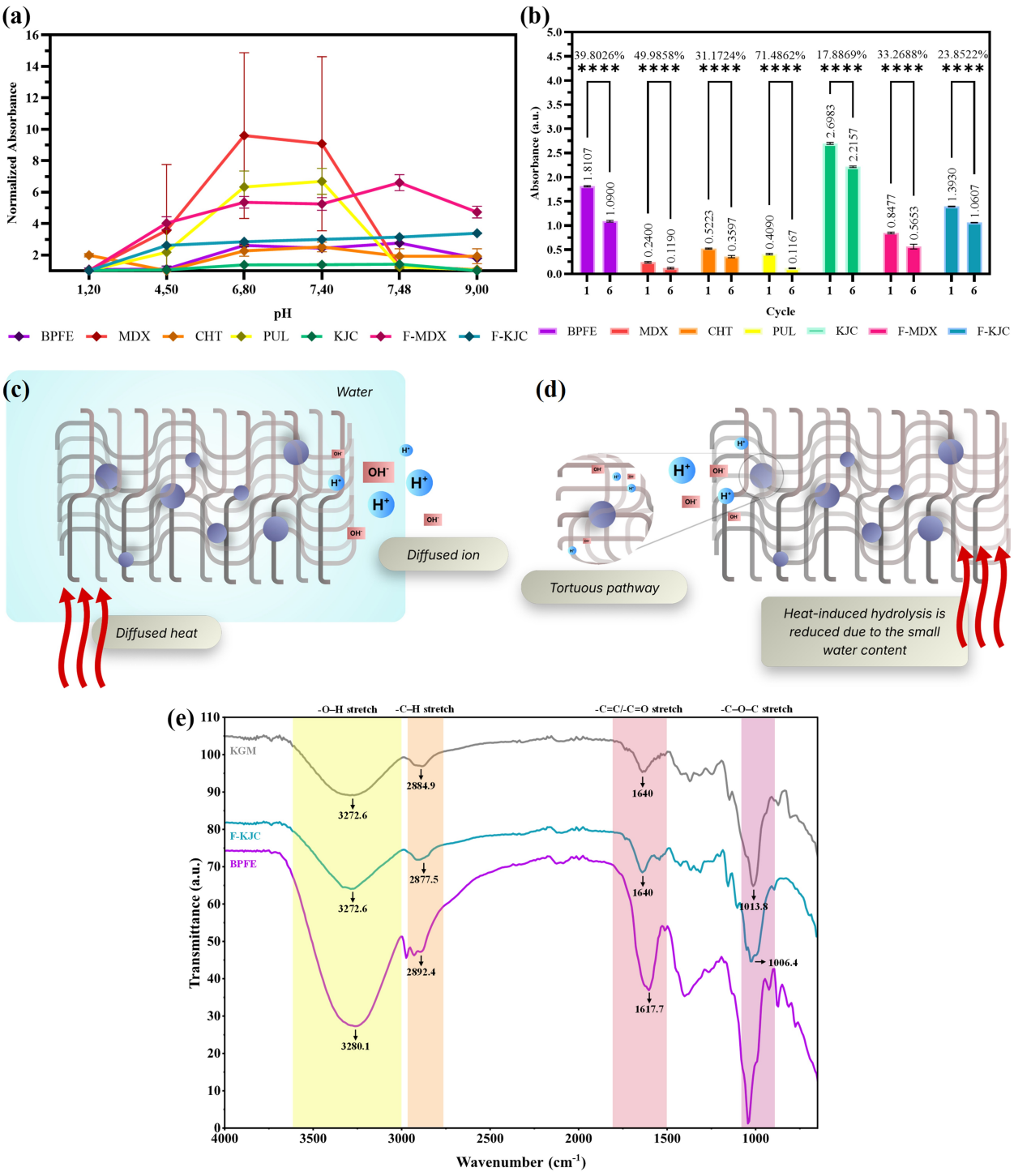

Figure 7. Stability of Stabilization Systems Under (a) pH Variation and (b) Thermodynamic cCycling, Possible Mechanism of (c) KJC and (d) F-KJC as Anthocyanin Stabilizer, and FTIR Spectra of BPFE and F-KJC Stabilization Systems

cycles. ANOVA with Tukey's multiple comparisons confirmed that all system pairs were significantly different at each cycle ($p < 0.0001$), indicating that stabilization type exerted a meaningful effect on absorbance retention. F-KJC achieved the second-lowest decline (23.85%), closely behind KJC (17.89%), while BPFE showed a 39.80% decline and PUL the worst

performance at 71.49%. The notably poor performance of PUL under thermodynamic cycling, despite its established film-forming barrier properties, is likely attributable to disruption of its linear glucan film network under repeated freeze-thaw stress, which compromises the structural integrity of the protective matrix. The relatively lower absolute absorbance of F-KJC and F-MDX compared to their gel counterparts at cycle 1 is attributed to changes in matrix physical properties after lyophilization, including increased porosity and possible partial anthocyanin aggregation during freezing and sublimation, which reduce light scattering in the redispersed system (Yang et al., 2017). Despite lower absolute values, F-KJC's more controlled rate of decline across cycles, combined with its superior pH consistency, establishes it as the most stable system overall, as the criterion of interest is resistance to degradation rather than absolute absorbance magnitude.

FTIR transmittance spectra of BPFE, F-KJC, and pure konjac glucomannan (KGM) powder were measured over 4000–650 cm^{-1}. As seen in Figure 7e, BPFE showed a broad O–H stretching band at ~3280 cm^{-1} associated with phenolic hydroxyl groups, an aromatic C=C/conjugated C=O band at ~1618 cm^{-1} characteristic of the flavylium chromophore, and a strong C–O glycosidic band at ~1006 cm^{-1} (Nurhayati et al., 2024). KGM showed a dominant O–H band at ~3273 cm^{-1} from its abundant hydroxyl groups, a C–H band at ~2885 cm^{-1}, and a C–O–C backbone band at ~1014 cm^{-1}, consistent with da Silva et al. (2020). The F-KJC spectrum showed a slight broadening and shift of the O–H band in the 3200–3400 cm^{-1} region compared to both BPFE and KGM individually, indicating the formation of intermolecular hydrogen bonds between the phenolic hydroxyl groups of anthocyanin and the mannose/glucose hydroxyl groups of KGM (Dong et al., 2023; Fu et al., 2023). The aromatic C=C/C=O band characteristic of anthocyanin (~1640 cm^{-1}) showed reduced intensity in F-KJC, consistent with intermolecular packing within the polysaccharide matrix restricting the vibrational freedom of the chromophore (Bhullar et al., 2022). Critically, no new peak appeared near ~1730 cm^{-1}, the region characteristic of ester C=O stretching, confirming that no covalent bond formation occurred during formulation. The C–O–C region (~1006–1014 cm^{-1}) showed a small inward shift in F−KJC relative to pure KGM, suggesting modification of the glycosidic linkage environment upon complexation. Collectively, these spectral changes categorize F−KJC as a physical complex stabilized by non-covalent interactions, primarily hydrogen bonding, without alteration of the fundamental chemical structures of either anthocyanin or konjac glucomannan. This non-covalent character is advantageous for a photosensitizer application, as it preserves the chromophoric integrity of the flavylium cation necessary for light absorption and ROS generation.

3.7 Singlet Oxygen Quantum Yield

Singlet oxygen ($^1O_2$) generation capacity was quantified using the 1,3-diphenylisobenzofuran (DPBF) photodegradation assay. DPBF is a highly selective singlet oxygen probe that reacts irreversibly with $^1O_2$ to form a non-absorbing endoperoxide intermediate, causing a measurable decline in absorbance at 410 nm; the rate of this decline is directly proportional to the rate of $^1O_2$ production (Entradas et al., 2020). Irradiation was performed using a 550 nm diode laser (0.1 W/cm^2, 1.434 cal) in both dark-protected and light-exposed conditions to distinguish true photodynamic activity from background auto-oxidation of DPBF (Canlica and Çetin, 2021). Methylene blue (MB, 1 ppm) was used as the positive control due to its well-characterized Type II photosensitizer activity and established quantum yield of $\Phi = 0.52$ (Silman et al., 2013). BPFE and F-KJC were tested at 1000 ppm, and 60% ethanol served as the negative control to confirm that DPBF degradation was attributable solely to photosensitizer activity rather than solvent effects.

Absorbance at 410 nm was recorded at 60-second intervals over 540 seconds. In dark-protected conditions, MB produced the fastest DPBF absorbance decline, followed by F−KJC and BPFE, while the negative control showed minimal change, confirming that DPBF degradation was driven by photosensitizer-mediated $^1O_2$ generation rather than spontaneous oxidation. In light-exposed conditions, the overall rate of DPBF decline was faster for all samples due to ambient light-driven photo-oxidation contributing additively to the photosensitizer effect; however, the relative ranking among samples remained consistent with dark conditions, confirming the validity of the results. The pseudo-first-order rate constant (k) was calculated from the slope of $\ln(A_0/A)$ versus irradiation time. Results are presented in Table 3. MB demonstrated the highest k values, followed by F−KJC, BPFE, and negative control. The coefficient of variation for F−KJC and BPFE remained below 7%, indicating good reproducibility, while the negative control showed higher variability (~50%) consistent with near-baseline noise rather than true activity.

The superior quantum yield of F-KJC relative to BPFE is perhaps mechanistically attributable to the low-moisture, mildly acidic microenvironment created by the freeze-dried konjac matrix. The native pH of BPFE was 3.22, while F-KJC measured pH 4.21 upon redispersion. At both pH values, anthocyanin predominantly exists as the flavylium cation, the photoactive form, which absorbs strongly in the 500–600 nm range (Radunz et al., 2020). However, the konjac matrix provides a physically constrained environment that reduces non-radiative energy dissipation by limiting molecular mobility, thereby increasing the probability of intersystem crossing (ISC) from the singlet excited state (S_1) to the triplet excited state (T_1). The T_1 state is the precursor for Type II energy transfer to ground-state molecular oxygen ($^3O_2$), generating $^1O_2$, the primary cytotoxic ROS in PDT (Oliveira et al., 2020). The reduced vibrational freedom of anthocyanin within the polysaccharide matrix thus may reduce non-radiative decay competing with ISC, potentially contributing to the higher observed quantum yield, though direct spectroscopic confirmation of band gap modification was not performed in this study and remains a subject for future investigation (Gao et al.,

Table 3. Pseudo-First-Order Rate Constant (k) Under Dark and Ambient Light Conditions

Sample	Dark	Ambient Light
Methylene blue (positive control)	$3.90 \times 10^{-4} \pm 3.35 \times 10^{-5}$	$4.51 \times 10^{-4} \pm 1.04 \times 10^{-4}$
F-KJC	$1.70 \times 10^{-4} \pm 1.11 \times 10^{-5}$	$4.41 \times 10^{-4} \pm 7.83 \times 10^{-5}$
BPFE	$2.54 \times 10^{-4} \pm 1.61 \times 10^{-5}$	$3.78 \times 10^{-4} \pm 2.09 \times 10^{-5}$
Ethanol 60% (negative control)	$3.56 \times 10^{-5} \pm 1.80 \times 10^{-5}$	$5.35 \times 10^{-5} \pm 5.52 \times 10^{-6}$

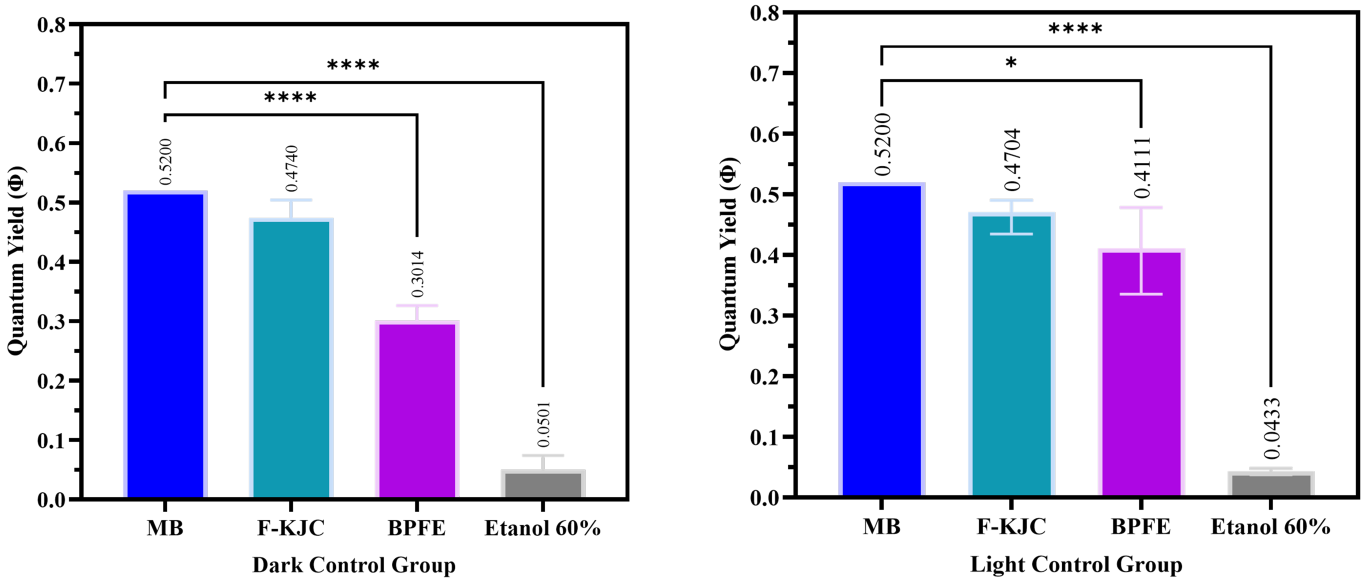

Figure 8. Quantum Yield Comparison Under Dark (Left) and Light (Right) Conditions for MB, F-KJC, BPFE, and Ethanol 60% (Negative Control)

2018).

This Type II photodynamic mechanism is consistent with the behaviour of MB, which operates via the same $S_1 \rightarrow T_1 \rightarrow {}^3O_2 \rightarrow {}^1O_2$ pathway (Silman et al., 2013), and aligns with observations by Lucioli et al. (2018) for anthocyanin-based dye-sensitized solar cells where intersystem crossing efficiency was linked to glycosylation pattern and chromophore rigidity. Although the quantum yields of BPFE and F-KJC remain below that of MB, this is expected since synthetic photosensitizers are typically optimized for heavy-atom-enhanced ISC, whereas natural anthocyanins rely solely on molecular orbital geometry. Nevertheless, the F-KJC quantum yield of 0.4740 is among the higher values reported for unmodified plant-derived photosensitizers, comparable to parietin ($\Phi = 0.69$) and hypocrelin ($\Phi = 0.47–0.62$) in class, though direct comparison is limited by differences in measurement conditions and irradiation wavelengths (Comini et al., 2017). Teerakapong et al. (2017) reported that cyanidin-3-glucoside (chrysanthemin) produces singlet oxygen with relatively low to moderate quantum yield but retains practical photosensitizer relevance due to its low dark toxicity and high biocompatibility, both properties that apply equally to the BPFE and F-KJC systems studied here.

3.8 Photothermal and Photodynamic Antibacterial Activity Against MRSA

The mechanisms by which PTT and PDT overcome resistant bacteria are illustrated in Figure 9c and 9d, respectively. In PTT, absorbed photons are dissipated as localized heat, raising the temperature at the bacterial surface to levels sufficient to increase cell membrane fluidity, disrupt membrane integrity, and denature proteins through hydrogen bond damage. In PDT, photoexcitation of the anthocyanin chromophore generates singlet oxygen ($^1O_2$), which damages bacteria through multiple simultaneous oxidative pathways including DNA damage, guanine base oxidation, protein denaturation, and disruption of membrane fatty acid double bonds (Bilici et al., 2020; Liu et al., 2015). The growth curve of MRSA showed a lag phase (2–4 h), transition to exponential growth (4–12 h), log phase (12–18 h), and stationary phase (18–24 h). OD-based antibacterial testing was performed with two laser wavelengths: 450 nm (photothermal) and 550 nm (photodynamic).

Under 450 nm irradiation, no significant difference was observed between irradiated and non-irradiated groups for both BPFE and F-KJC across most time points as shown in Figure 9a, confirmed by Tukey multiple comparisons analy-

sis. The absence of a photothermal enhancement is primarily attributed to insufficient energy deposition: the 450 nm laser delivered a total heat energy of 21.510 cal during the irradiation window, which is unlikely to raise local bacterial culture temperature to the established bactericidal threshold of approximately 45–50°C required for membrane lipid phase transition, protein denaturation, and consequent irreversible cell death (Ziesmer et al., 2023). Photothermal inactivation of bacteria is fundamentally dependent on achieving a critical temperature elevation within a defined exposure time; below this threshold, sub-lethal thermal stress may transiently impair bacterial metabolism without producing bactericidal outcomes (Chen et al., 2020). Furthermore, blue light at 450 nm has limited tissue and liquid penetration depth relative to near-infrared wavelengths, which further reduces the effective energy delivered to bacteria suspended in culture medium (Ferrer-Espada et al., 2020). It should also be noted that anthocyanins are more efficiently photoexcited at wavelengths corresponding to their absorption maximum (~550–600 nm for the flavylium cation), meaning that 450 nm irradiation may not optimally activate the chromophore for either photothermal conversion or ROS generation, resulting in a dual inefficiency for this wavelength under the experimental conditions used.

Both irradiated and non-irradiated BPFE and F-KJC groups nonetheless exhibited growth suppression relative to the negative control throughout the 24-hour observation period, with F-KJC consistently producing lower OD values than BPFE. This intrinsic antibacterial activity, independent of irradiation, reflects the well-documented anti-staphylococcal properties of *C. ternatea* anthocyanins, particularly the ternatin series, which disrupt bacterial membrane integrity and interfere with cell wall synthesis at concentrations achievable with the 8% extract used (Jeyaraj et al., 2022). The lower OD of F-KJC relative to BPFE without irradiation may suggest that the freeze-dried konjac matrix could influence the release profile of anthocyanin in the culture medium, potentially maintaining effective local concentrations throughout the incubation period. However, release kinetics were not directly measured in this study and this interpretation requires further confirmation (Xue et al., 2024).

Under 550 nm irradiation, both BPFE and F-KJC produced significantly lower MRSA OD growth curves compared with their respective non-irradiated counterparts, particularly for F-KJC, as shown in Figure 9b, with differences confirmed as statistically significant by Tukey multiple comparisons at multiple time points. The 550 nm wavelength corresponds closely to the absorption maximum of the anthocyanin flavylium cation, enabling efficient photoexcitation and ROS generation that may damage multiple bacterial targets including membrane phospholipids, cell wall peptidoglycans, and nucleic acids through oxidative stress. This multi-target oxidative mechanism has been proposed as a basis for the low likelihood of resistance development against PDT-based approaches compared with conventional antibiotics, though this was not directly evaluated in the present study (Liu et al., 2015). The superior photodynamic performance of F-KJC over BPFE under 550 nm irradiation is consistent with its higher singlet oxygen quantum yield ($\Phi = 0.4740$ vs. $\Phi = 0.3014$) as established in the DPBF assay. The improved quantum yield of F-KJC is likely related to the stabilization of the flavylium cation form of anthocyanin within the freeze-dried konjac matrix, which maintains a microenvironment of low water activity and mild acidity that may favor intersystem crossing efficiency (Radunz et al., 2020). The FTIR evidence of non-covalent hydrogen bonding between anthocyanin and KGM chains in the F-KJC complex further suggests that restricted molecular mobility within the matrix may reduce non-radiative quenching, consistent with observations for other polysaccharide-encapsulated chromophores (Dong et al., 2022). Astuti et al. (2024) similarly reported that laser activation of *C. ternatea*-derived silver nanoparticles substantially amplified antibacterial efficacy beyond the intrinsic extract activity, supporting the general observation that photoactivation can enhance antibacterial effects of *C. ternatea*-derived systems.

Non-irradiated BPFE and F-KJC groups still exhibited partial MRSA growth suppression relative to the negative control, consistent with the intrinsic antibiofilm and anti-MRSA activity of *C. ternatea* anthocyanins documented by Hamzah et al. (2024), who reported perturbation of extracellular polymeric substance components upon extract treatment. The observed combination of baseline antibacterial activity and laser-activated growth inhibition under 550 nm irradiation suggests a potentially complementary dual-action profile, where intrinsic anthocyanin activity and photodynamic ROS generation may act through distinct but concurrent mechanisms; however, whether these effects are additive or synergistic was not formally evaluated in this study and would require dedicated combination assays to confirm (Saba et al., 2025). The inability of 450 nm irradiation to replicate this enhancement, despite the extract exhibiting photothermal conversion capacity in earlier experiments, underscores that both wavelength selection and irradiance parameters must be optimized concurrently for effective PTT, and that future studies should consider higher power densities or pulsed irradiation protocols to achieve the temperature thresholds required for bactericidal photothermal effects (Chen et al., 2020; Overchuk et al., 2023).

It should be clarified that the OD-based measurements in this study assess bacterial growth inhibition rather than conversion of resistant to non-resistant phenotype. Conversion of MRSA to methicillin-susceptible *S. aureus* (MSSA) would require loss or suppression of the *mecA* gene or PBP2a expression, which is not assessed by turbidimetric methods. PDT-mediated ROS generation causes oxidative damage to multiple cellular targets including membrane lipids, proteins, and nucleic acids, which may reduce bacterial viability and proliferation capacity without necessarily altering the genetic resistance determinants (Liu et al., 2015). Whether sub-lethal PDT exposure could induce phenotypic changes in PBP2a expression or *mecA* transcription is a question beyond the scope of the present study and would require molecular bacteriology methods such as qRT-PCR or Western blot analysis of PBP2a expression. The

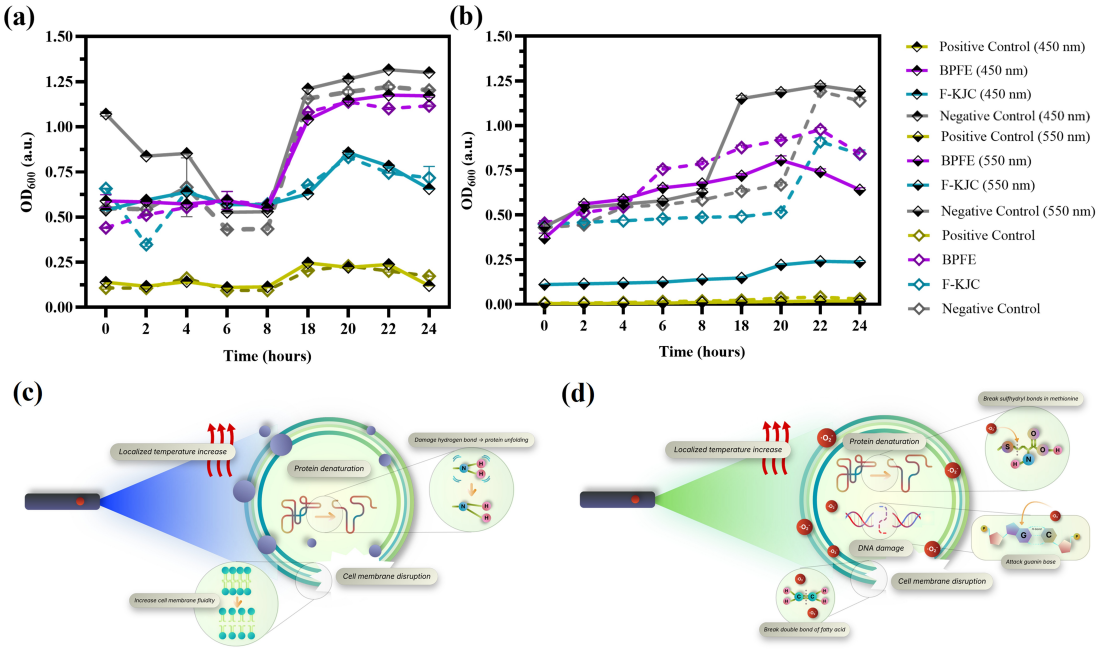

Figure 9. Optical Density Growth Curves of MRSA Under (a) 450 nm and (b) 550 nm Laser Irradiation for Photothermal and Photodynamic Assessment, with Schematic Diagram of (c) Photothermal and (d) Photodynamic Activity Against Bacteria

results of this study therefore support *C. ternatea* anthocyanin as a growth inhibitor of MRSA under photodynamic conditions, not as a resistance-reversal agent.

4. CONCLUSION

This study investigated the stabilization of butterfly pea (*Clitoria ternatea*) anthocyanin extract using polysaccharide-based systems and evaluated their potential as natural photosensitizers for PTT/PDT against MRSA through complementary *in silico* and *in vitro* approaches. Dried flower extraction yielded a total anthocyanin content of 5.037 ± 0.395 mg CGE/L-approximately 2.08-fold higher than fresh flower extract-with a photothermal efficiency of 52.34 ± 7.93% at 450 nm, consistent with the strong π–π^* absorption of acylated delphinidin derivatives at this wavelength. Molecular docking against PBP2a revealed that 16 of 18 screened *C. ternatea* compounds surpassed the native ligand binding affinity, with Preternatin C4, kaempferol 3-*O*-robinobioside, and kaempferol 3-rutinoside achieving the strongest affinities (−11.1 and −11.0 kcal/mol), engaging key catalytic residues including SER-403, ASN-464, GLN-521, and THR-600-suggesting potential for PBP2a-mediated antibacterial activity that warrants experimental confirmation. The extract at 8% demonstrated moderate antibacterial activity against *S. aureus* (10.67 ± 0.94 mm inhibition zone), consistent with the membrane-disrupting and cell wall-interfering properties reported for *C. ternatea* ternatin derivatives. Among the stabilization systems evaluated, F-KJC achieve d the most consistent absorbance profile across all six pH conditions and the second-lowest thermodynamic degradation (23.85%), supported by FTIR evidence of non-covalent hydrogen bonding between anthocyanin and konjac glucomannan chains. F-KJC also exhibited a higher singlet oxygen quantum yield (Φ = 0.4740) compared with BPFE (Φ = 0.3014), consistent with the matrix-induced restriction of molecular mobility reducing non-radiative decay competing with intersystem crossing. Under 550 nm photodynamic irradiation, F-KJC significantly inhibited MRSA growth relative to non-irradiated controls, while 450 nm photothermal irradiation did not produce a statistically significant enhancement under the applied conditions, attributed to insufficient energy deposition and suboptimal chromophore excitation at this wavelength. Collectively, these results support the freeze-dried konjac glucomannan system as a promising stabilization strategy for butterfly pea anthocyanin photosensitizers, with *in vitro* proof-of-concept established for photodynamic activity against MRSA. Future work should include LC-MS metabolite profiling, cytotoxicity evaluation, molecular docking against additional MRSA-associated receptors, and *in vivo* studies to further establish therapeutic potential.

5. ACKNOWLEDGMENT

The author thanks the supervisors and examiners at the Department of Pharmacy, Universitas Sriwijaya, for their guidance. The author acknowledges Herbarium Andalas (ANDA), Universitas Andalas, for herbarium identification, and the UPT Integrated Laboratory of Universitas Lampung for FTIR analysis.

This research was supported by the Department of Pharmacy, Faculty of Mathematics and Natural Sciences, Universitas Sriwijaya.

REFERENCES

Alappat, B. and J. Alappat (2020). Anthocyanin Pigments: Beyond Aesthetics. *Molecules*, **25**(23); 5500

Arsyad, W. O. S., O. S. Wijaya, I. Usman, I. Saleh, M. H. Al Rasyid, and Y. Sari (2025). Analisis Spektrum Absorbansi dan Identifikasi Fitokimia dari Fraksi Bunga Telang (*Clitoria ternatea* L.) sebagai Penyerap Cahaya dalam Dye-Sensitized Solar Cell (DSSC). *Jurnal Aplikasi Fisika*, **21**(2); 1–15

Astuti, S. D., R. A. F. Ghinaa, M. U. S. Umaimah, R. Aisya, A. H. Zaidan, and A. K. Yaqubi (2024). Red Laser-Activated Silver Nanoparticles from Green Synthesis Extract of Butterfly Pea for Antimicrobial Photodynamic Therapy Against *Staphylococcus aureus*. *Indonesian Journal of Tropical and Infectious Disease*, **12**(3); 237–251

Azzahra, F. D., L. N. Mulyani, T. Sabrina, and N. A. Fithri (2025). Liposome Photosensitizer with Enzyme from Black Soybean Tempeh: Formula Optimization and In Vitro Thrombolytic Activity Evaluation. *Science and Technology Indonesia*, **10**; 903–915

Bhullar, K. A., M. I. Horgan, A. Le, D. Fania, R. Wuhrer, V. Razmovski-Naumovski, K. Chan, P. Castignolles, and M. Gaborieau (2022). Assessing the Quantification of Acetylation in Konjac Glucomannan Via ATR-FTIR and Solid-state NMR Spectroscopy. *Carbohydrate Polymers*, **291**; 119659

Bilici, K., N. Atac, A. Muti, I. Baylam, O. Dogan, and H. Yagci Acar (2020). Broad Spectrum Antibacterial Photodynamic and Photothermal Therapy Achieved with Indocyanine Green Loaded SPIONs Under Near Infrared Irradiation. *Biomaterials Science*, **8**(16); 4616–4625

Bissantz, C., B. Kuhn, and M. Stahl (2010). A Medicinal Chemist's Guide to Molecular Interactions. *Journal of Medicinal Chemistry*, **53**(14); 5061–5084

Bresolí-Obach, R., J. Torra, R. P. Zanocco, A. L. Zanocco, and S. Nonell (2021). Singlet Oxygen Quantum Yield Determination Using Chemical Acceptors. In *Methods in Molecular Biology*, volume 2202. pages 165–188

Canlica, M. and İ. Çetin (2021). Anticancer Activities of a Metal-Free Phthalocyanine on MCF-7 and MDA-MB-231 Cells and Singlet Oxygen Production as a Photosensitizer in PDT. *Journal of the Turkish Chemical Society Section A: Chemistry*, **8**(4); 1025–1034

Chen, Y., Y. Gao, Y. Chen, L. Liu, A. Mo, and Q. Peng (2020). Nanomaterials-Based Photothermal Therapy and Its Potentials in Antibacterial Treatment. *Journal of Controlled Release*, **328**; 251–262

Comini, L. R., F. E. Morán Vieyra, R. A. Mignone, P. L. Páez, M. Laura Mugas, and C. D. Borsarelli (2017). Parietin: An Efficient Photo-Screening Pigment In Vivo with Good Photosensitizing and Photodynamic Antibacterial Effects In Vitro. *Photochemical & Photobiological Sciences*, **16**(2); 201–210

da Silva, D. F., C. Y. L. Ogawa, F. Sato, A. M. Neto, F. H. Larsen, and P. T. Matumoto-Pintro (2020). Chemical and Physical Characterization of Konjac Glucomannan-Based Powders by FTIR and ^{13}C MAS NMR. *Powder Technology*, **361**; 610–616

Dai, T., G. P. Tegos, T. Zhiyentayev, E. Mylonakis, and M. R. Hamblin (). Photodynamic Therapy for Methicillin-Resistant *Staphylococcus aureus* Infection in a Mouse Skin Abrasion Model

Dighriri, I. M., S. Alanazi, K. AlMutairi, S. J. Alhusayni, F. M. Balharith, and A. M. Alansari (2025). Efficacy and Safety of Vancomycin, Linezolid, and Ceftaroline in the Treatment of Methicillin-Resistant *Staphylococcus aureus* (MRSA): A Systematic Review and Meta-Analysis. *Cureus*, **17**(1); e77949

Dong, R., J. Tian, Z. Huang, Q. Yu, J. Xie, and Y. Chen (2023). Intermolecular Binding of Blueberry Anthocyanins with Water-Soluble Polysaccharides: Enhancing Their Thermostability and Antioxidant Abilities. *Food Chemistry*, **410**; 135375

Dong, W., X. Yang, N. Zhang, P. Chen, J. Sun, and M. Zhang (2024). Study of UV–Vis Molar Absorptivity Variation and Quantitation of Anthocyanins Using Molar Relative Response Factor. *Food Chemistry*, **444**; 138653

Dong, Y., C. Yang, W. Zhong, Y. Shu, Y. Zhang, and D. Yang (2022). Antibacterial Effect and Mechanism of Anthocyanin from *Lycium ruthenicum* Murr. *Frontiers in Microbiology*, **13**; 974602

Edityaningrum, C. A., N. A. Fithri, L. H. Nurani, W. Widyaningsih, B. S. Zaelifa, and R. D. N. Marrisca (2026). Innovation of Avocado (*Persea americana* Mill.) Leaf Extract Patch for Diabetic Wound Treatment: An In Silico and In Vivo Investigation. *Pharmacia*, **73**; e178290

Entradas, T., S. Waldron, and M. Volk (2020). The Detection Sensitivity of Commonly Used Singlet Oxygen Probes in Aqueous Environments. *Journal of Photochemistry and Photobiology B: Biology*, **204**; 111787

Ferrer-Espada, R., Y. Wang, X. S. Goh, and T. Dai (2020). Antimicrobial Blue Light (405-nm) Inactivation of Microbial Isolates in Biofilms. *Lasers in Surgery and Medicine*, **52**(5); 472–478

Fishovits, J., J. A. Hermoso, M. Chang, and S. Mobashery (2014). Penicillin-Binding Protein 2a of Methicillin-Resistant *Staphylococcus aureus*. *IUBMB Life*, **66**(8); 572–577

Fithri, N. A., Mardiyanto, A. Fadilah, A. Pratiwi, S. S. Alisyahbana, and N. P. Maharani (2025). Uncaria Gambir Based Green Synthesis of Inorganic Nanoparticles for Photothermal Induced Thrombolytic and Antibacterial Applications. *Science and Technology Indonesia*, **10**; 303–312

Fithri, N. A., L. N. Mulyani, T. Sabrina, F. D. Azzahra, R. S. Linthra, and M. Akram (2026). Liposomal Formulation of Plant Based Natural Photosensitisers for Thrombosis. *Indonesian Journal of Pharmacy*; 367–380

Fithri, N. A., Y. Wu, G. Cowin, F. Akther, H. D. N. Tran, and

H. T. Ta (2023). Gold-Iron Oxide Nanoparticle: A Unique Multimodal Theranostic Approach for Thrombosis. *Applied Materials Today*, **31**; 101750

Fu, W., S. Li, H. Helmick, B. R. Hamaker, J. L. Kokini, and L. Reddivari (2023). Complexation with Polysaccharides Enhances the Stability of Isolated Anthocyanins. *Foods*, **12**(9); 1846

Gao, R., X. Mei, D. Yan, R. Liang, and M. Wei (2018). Nano-Photosensitizer Based on Layered Double Hydroxide and Isophthalic Acid for Singlet Oxygenation and Photodynamic Therapy. *Nature Communications*, **9**(1); 2798

Gomaa, A. A. R., H. A. Abou-Zied, S. M. Farhan, R. I. Bedaiwi, M. A. Alanazi, and E. R. Abdelaleem (2025). *Apium graveolens*-Associated *Aspergillus* sp.: Metabolomic Profiling and Anti-MRSA Potential Supported by In Silico Studies. *Microbial Cell Factories*, **24**(1); 57

Gonçalves, L. C. P. (2021). Photophysical Properties and Therapeutic Use of Natural Photosensitizers. *Journal of Photochemistry and Photobiology*, **7**; 100052

Hamzah, H., S. U. T. Pratiwi, A. Nur, T. Nuryastuti, V. Y. Pratama, and R. Maulana (2024). Antibacterial and Antibiofilm Activities of Ternate Blue Pea (*Clitoria ternatea*) Flower Extract Against *Staphylococcus aureus*. *Tropical Journal of Natural Product Research*, **8**(1); 5992–5996

Handayani, L., S. Aprilia, N. Arahman, and M. R. Bilad (2024). Identification of the Anthocyanin Profile from Butterfly Pea (*Clitoria ternatea* L.) Flowers Under Varying Extraction Conditions: Evaluating Its Potential as a Natural Blue Food Colorant and Its Application as a Colorimetric Indicator. *South African Journal of Chemical Engineering*, **49**; 151–161

Ikhwanurridlo, A., I. A. K. Aji, Y. Nindita, V. Karlowee, E. Mahati, and N. Susilaningsih (2025). Comparative Analysis of Anthocyanin and Flavonoid Content in *Clitoria ternatea* L. Using an Ultrasonic-Assisted Extraction Approach. *Plant Trends*, **3**(4); 114–121

Jeyaraj, E. J., Y. Y. Lim, and W. S. Choo (2022). Antioxidant, Cytotoxic, and Antibacterial Activities of *Clitoria ternatea* Flower Extracts and Anthocyanin-Rich Fraction. *Scientific Reports*, **12**(1); 14890

Khoo, H. E., A. Azlan, S. T. Tang, and S. M. Lim (2017). Anthocyanidins and Anthocyanins: Colored Pigments as Food, Pharmaceutical Ingredients, and the Potential Health Benefits. *Food & Nutrition Research*, **61**(1); 1361779

Kong, C. and X. Chen (2022). Combined Photodynamic and Photothermal Therapy and Immunotherapy for Cancer Treatment: A Review. *International Journal of Nanomedicine*, **17**; 6427–6446

Kraśniewska, K., I. Ścibisz, M. Gniewosz, M. Mitek, K. Pobiega, and A. Cendrowski (2017). Effect of Pullulan Coating on Postharvest Quality and Shelf-Life of Highbush Blueberry (*Vaccinium corymbosum* L.). *Materials*, **10**(8); 965

Lee, J., R. W. Durst, and R. E. Wrolstad (2005). Determination of Total Monomeric Anthocyanin Pigment Content of Fruit Juices, Beverages, Natural Colorants, and Wines by the pH Differential Method: Collaborative Study. *Journal of AOAC International*, **88**(5); 1269–1278

Li, L. and Q. Li (2025). Advancements in Chitosan–Anthocyanin Composite Films: Sustainable Food Preservation with Biodegradable Packaging. *Foods*, **14**(10); 1721

Liu, Y., R. Qin, S. A. J. Zaat, E. Breukink, and M. Heger (2015). Antibacterial Photodynamic Therapy: Overview of a Promising Approach to Fight Antibiotic-Resistant Bacterial Infections. *Journal of Clinical and Translational Research*, **1**(3); 140–167

Lucioli, S., C. Di Bari, C. Forni, A. Di Carlo, E. Barrajón-Catalán, and E. Caboni (2018). Anthocyanic Pigments from Elicited In Vitro Grown Shoot Cultures of *Vaccinium corymbosum* L., cv. Brigitta Blue, as Photosensitizer in Natural Dye-Sensitized Solar Cells (NDSSC). *Journal of Photochemistry and Photobiology B: Biology*, **188**; 69–76

Mardiyanto, M., I. Sholihah, and T. G. Jaya (2020). The Chitosan-Sodium Alginate Submicro Particles Loading Herbal of Ethanolic Extract of Leaves *Senna alata* L. for Curing of Bacterial Infection on Skin. *Science and Technology Indonesia*, **5**(3); 85–89

Marpaung, A. M. and D. Pustikarini (2023). Spectrophotometric Change of Butterfly Pea (*Clitoria ternatea* L.) Flower Extract in Various Metal Ion Solutions During Storage. *Science and Technology Indonesia*, **8**(3); 367–372

Navarro-Pérez, M. L., M. C. Fernández-Calderón, and V. Vadillo-Rodríguez (2022). Decomposition of Growth Curves into Growth Rate and Acceleration: A Novel Procedure to Monitor Bacterial Growth and the Time-Dependent Effect of Antimicrobials. *Applied and Environmental Microbiology*, **88**(4); e01849–21

Nurhayati, R., F. Shoviantari, T. E. Munandar, and M. Yuwono (2024). Butterfly Pea (*Clitoria ternatea* L.) Flower Water and Ethanol Extract: Phytochemical Screening, FTIR Analysis, and Antioxidant Activity Estimation Using Comparison of ABTS, DPPH, and FRAP Assays. *Research Journal of Pharmacy and Technology*, **17**(5); 1973–1982

Oguis, G. K., E. K. Gilding, M. A. Jackson, and D. J. Craik (2019). Butterfly Pea (*Clitoria ternatea*), a Cyclotide-Bearing Plant with Applications in Agriculture and Medicine. *Frontiers in Plant Science*, **10**; 645

Oliveira, H., P. Correia, A. R. Pereira, P. Araújo, N. Mateus, and I. Fernandes (2020). Exploring the Applications of the Photoprotective Properties of Anthocyanins in Biological Systems. *International Journal of Molecular Sciences*, **21**(20); 7464

Otero, L. H., A. Rojas-Altuve, L. I. Llarrull, C. Carrasco-López, M. Kumarasiri, and J. A. Hermoso (2013). How Allosteric Control of *Staphylococcus aureus* Penicillin-Binding Protein 2a Enables Methicillin Resistance and Physiological Function. *Proceedings of the National Academy of Sciences*, **110**(42); 16808–16813

Overchuk, M., R. A. Weersink, B. C. Wilson, and G. Zheng (2023). Photodynamic and Photothermal Therapies: Synergy Opportunities for Nanomedicine. *ACS Nano*, **17**(8); 7979–7997

Ozcelik, M. and U. Kulozik (2023). The Role of Maltodextrin Concentration in Maintaining Storage Stability of Dried Fruit Foams Texturized Using Plant Protein–Polysaccharide Blends. *Foods*, **12**(8); 1673

Polat, E. and K. Kang (2021). Natural Photosensitizers in Antimicrobial Photodynamic Therapy. *Biomedicines*, **9**(6); 584

Purnamayanti, A., K. Budipramana, and M. E. Gondokesumo (2022). The Potential Application of *Clitoria ternatea* for Cancer Treatment. *Pharmaceutical Sciences and Research*, **9**(3); 109–124

Putra, T., T. N. M. Zainol, M. K. Mohdisa, and N. Mohdmaidin (2021). Chemical Characterization of Ethanolic Extract of Butterfly Pea Flower (*Clitoria ternatea*). *Food Research*, **5**(4); 127–134

Radunz, S., S. Wedepohl, M. Röhr, M. Calderón, H. R. Tschiche, and U. Resch-Genger (2020). pH-Activatable Singlet Oxygen-Generating Boron-Dipyrromethenes (BODIPYs) for Photodynamic Therapy and Bioimaging. *Journal of Medicinal Chemistry*, **63**(4); 1699–1708

Ramadhani, F. A., M. F. Prastika, N. Fikriyah, Isnaeni, and N. W. Diyah (2024). Molecular Docking of Flavonoids from Extract of Roselle (*Hibiscus sabdariffa* L.) Calyx on PBP2a as the Basis for Antibacterial Activity Against Methicillin-Resistant *Staphylococcus aureus*. *Science and Technology Indonesia*, **9**(2); 487–493

Roper, D. K., W. Ahn, and M. Hoepfner (2007). Microscale Heat Transfer Transduced by Surface Plasmon Resonant Gold Nanoparticles. *The Journal of Physical Chemistry C*, **111**(9); 3636–3641

Saba, S. S., S. Ghivari, M. Pujar, and U. Maggavi (2025). Antibacterial Efficacy of Herbal Extracts as Photosensitizers in Photodynamic Root Canal Disinfection. *Journal of Conservative Dentistry and Endodontics*, **28**(5); 420–425

Shen, Y., L. Du, H. Zeng, X. Zhang, W. Prinyawiwatkul, and Z. Xu (2016). Butterfly Pea (*Clitoria ternatea*) Seed and Petal Extracts Decreased HEp-2 Carcinoma Cell Viability. *International Journal of Food Science and Technology*, **51**(8); 1860–1868

Shivanika, C., S. Deepak Kumar, V. Ragunathan, P. Tiwari, A. Sumitha, and P. Brindha Devi (2022). Molecular Docking, Validation, Dynamics Simulations, and Pharmacokinetic Prediction of Natural Compounds Against the SARS-CoV-2 Main Protease. *Journal of Biomolecular Structure and Dynamics*, **40**(2); 585–611

Silman, I., E. Roth, A. Paz, M. M. Triquigneaux, M. Ehrenshaft, and L. Weiner (2013). The Specific Interaction of the Photosensitizer Methylene Blue with Acetylcholinesterase Provides a Model System for Studying the Molecular Consequences of Photodynamic Therapy. *Chemico-Biological Interactions*, **203**(1); 63–70

Solihah, I., M. Mardiyanto, S. Fertilita, H. Herlina, and O. Charmila (2018). The Standardization of Ethanolic Extract of Tahongai Leaves (*Kleinhovia hospita* L.). *Science and Technology Indonesia*, **3**(1); 14–18

Syahniar, R., Rayhana, D. S. Kharisma, M. Khatami, and D. B. B. Duarsa (2020). Methicillin-Resistant *Staphylococcus aureus* Among Clinical Isolates in Indonesia: A Systematic Review. *Biomedical and Pharmacology Journal*, **13**(4); 1871–1878

Takeno, H., R. Hashimoto, Y. Lu, and W.-C. Hsieh (2022). Structural and Mechanical Properties of Konjac Glucomannan Gels and Influence of Freezing-Thawing Treatments on Them. *Polymers*, **14**(18); 3703

Teerakapong, A., T. Damrongrungruang, S. Sattayut, N. P. Morales, and S. Tantananugool (2017). Efficacy of Erythrosine and Cyanidin-3-Glucoside Mediated Photodynamic Therapy on Porphyromonas gingivalis Biofilms Using Green Light Laser. *Photodiagnosis and Photodynamic Therapy*, **20**; 154–158

Thuy, N. M., T. C. Ben, V. Quang Minh, and N. Van Tai (2021). Effect of Extraction Techniques on Anthocyanin from Butterfly Pea Flowers (Clitoria ternatea L.) Cultivated in Vietnam. *Journal of Applied Biology & Biotechnology*, **9**(6); 173–180

Tong, S. Y. C., J. S. Davis, E. Eichenberger, T. L. Holland, and V. G. Fowler (2015). Staphylococcus aureus Infections: Epidemiology, Pathophysiology, Clinical Manifestations, and Management. *Clinical Microbiology Reviews*, **28**(3); 603–661

Wong, T. W., S. Z. Liao, W. C. Ko, C. J. Wu, S. B. Wu, and I. H. Huang (2019). Indocyanine Green-Mediated Photodynamic Therapy Reduces Methicillin-Resistant Staphylococcus aureus Drug Resistance. *Journal of Clinical Medicine*, **8**(3); 411

Wrolstad, R. E., R. W. Durst, and J. Lee (2005). Tracking Color and Pigment Changes in Anthocyanin Products. *Trends in Food Science & Technology*, **16**(9); 423–428

Xue, H., J. Zhao, Y. Wang, Z. Shi, K. Xie, and J. Tan (2024). Factors Affecting the Stability of Anthocyanins and Strategies for Improving Their Stability: A Review. *Food Chemistry: X*, **24**; 101883

Yang, D., Y. Yuan, L. Wang, X. Wang, R. Mu, and Y. Zheng (2017). A Review on Konjac Glucomannan Gels: Microstructure and Application. *International Journal of Molecular Sciences*, **18**(11); 2250

Yanti, N. L. P. K. M., Sukrasno, D. Rizaldy, and A. Al Iman (2022). Profiling Secondary Metabolite of Fresh and Fermented Marigold Flowers and Butterfly Pea Flowers. *Ad-Dawaa' Journal of Pharmaceutical Sciences*, **5**(2); 140–156

Ziesmer, J., J. V. Larsson, and G. A. Sotiriou (2023). Hybrid Microneedle Arrays for Antibiotic and Near-IR Photothermal Synergistic Antimicrobial Effect Against Methicillin-Resistant Staphylococcus aureus. *Chemical Engineering Journal*, **462**; 142127

